The following manuscript is a non-peer reviewed preprint that has been invited for submission to the Geological Society of London Special Publication entitled "*A Tour of the Solid Solar System: Recognizing Early Career Contributions to Extraterrestrial Geology*" on October 1st, 2024. It is in prep for submission as of October 14th, 2024.

The evidence for open magmatic system processes recorded in the crystal cargoes of lunar basalts 10057, 12038, 12043, 15085, 15556, and 70017

A. J. Gawronska[1*†], C. L. McLeod[1], M. Loocke[2], B. Shaulis[3]

[1]Department of Geology and Environmental Earth Science, Miami University, Oxford OH, 45056

[2]Chevron Geomaterials Characterization Laboratory, Department of Geology and Geophysics, Louisiana State University, Baton Rouge LA

[3]Trace Element and Radiogenic Isotope Laboratory, University of Arkansas, Fayetteville AR

*Corresponding author: ajvgawronska@gmail.com

†Current affiliation: [1]Physics Department, Catholic University of America, Washington D. C., 20064, [2]NASA Goddard Space Flight Center, Greenbelt MD, 20770.

Abstract

Basaltic magmatism is fundamental to planetary evolution, and continues to be studied in depth on Earth. Terrestrial studies indicate that basaltic magmatic systems are generally comprised of a series of batches with distinct compositions, which can be stored at depth within crystal frameworks, creating mushes. The crystal cargos of magmas erupted from such systems record evidence of the mush environment from which they crystallized, and the processes that worked to mobilize them. Here, we investigated if and how this relates to extraterrestrial magmatic systems by studying the textures and compositions at the crystal scale of basaltic samples collected during the Apollo missions. We found that four out of six samples studied here contain cargos that have reaction textures and reverse zoning, which are interpreted here as denoting an antecrystic origin. Specifically, pyroxene cargos in 10057, 12043, 15085, and 70017 contain grains that are sieved, resorbed, and broken down into symplectite, alongside grains that do not record such disequilibrium textures. The same pyroxene grains often record elevated trace element contents and/or reverse zoning in Mg and Cr relative to other grains, suggesting distinct petrogenetic histories. These four samples additionally contain feldspars reversely zoned in elements like An and Sr alongside grains normally zoned in these elements, indicating the existence of multiple population as a result of changing melt conditions. The textures and chemistries seen in the four samples are consistent with generation in a system whose architecture includes distinct magma lenses where magmas were stored as mushes, and may have been transported between lenses via porous flow and mobilized by influx of hot, primitive magma. Future work should evaluate individual lunar magmatic systems in greater detail to investigate the influence of these processes further.

1 Introduction

1.1 Insights from terrestrial systems on basaltic magmatism

Basaltic magmatism is a fundamental process of planetary differentiation, evolution, and crustal (re)surfacing (BVSP, 1981, Wilson, 2009). As direct products of mantle partial melting, basaltic lavas have provided a wealth of information regarding the make-up and evolution of Earth's mantle, the generation of secondary basaltic crusts, and the architecture of magmatic systems and processes operating within them. This has been made possible through decades of detailed mineralogical, textural, geochemical, and geochronological analyses, coupled with observations over a range of temporal and spatial scales thanks to detailed interdisciplinary analyses (BVSP, 1981; Jerram and Davidson, 2007; Lee et al., 2009; Marsh et al., 2009; Cashman et al., 2015; 2017; Middlemost, 2014; Ogawa, 2018; Edmonds et al., 2019; Sparks et al., 2019). Recent 10^2 to 10^3 m-scale geophysical investigations of terrestrial magmatic systems indicate that magmas are generally not stored in large-scale chambers (see recent discussions by Edmonds et al., 2019; Sparks et al., 2019; Paulatto et al., 2022). Recent work suggests this is also true at hotspot volcanoes such as Hawai'i (Wilding et al., 2023), which is often invoked as one of the best analogs for lunar mare eruption dynamics (i.e., Head, 1976; Spudis et al., 2013). Instead, the study of crystal cargoes in magmatic products has recently led to a "paradigm shift" in the field of igneous petrology and an advancement in our understanding of magma plumbing system architecture. Through detailed textural and microgeochemical analysis, researchers have recognized that magmas are stored as distinct batches within lenses, which connect to form trans-crustal magmatic systems (e.g., Cashman et al., 2017; Edmonds et al., 2019; Sparks et al., 2019). In this framework, magma batches evolve separately and produce crystal cargoes which record unique petrogenetic histories. As they cool, melts produce crystal frameworks – the resulting interstitial melts stored in crystal frameworks are defined as "mushes" (Cashman et al., 2017; Sparks et al., 2019). Upon remobilization during transport and ascent, batches have the potential to mix and mingle, exchanging molten (liquid) and solidified (crystals) material to produce a new carrier (or host) magma with a distinct cargo (Fig. 1; i.e., Cashman et al., 2017; Edmonds et al., 2019; Sparks et al., 2019, and references therein). Additional contamination of the carrier magma by surrounding wall rock can further influence final whole rock compositions. As a result, the whole rock compositions of lavas erupted at the surface are not always direct indicators of their source regions but more so of physical mechanisms that work to change magma composition over time (i.e., mixing, assimilation, fractionation; Blundy and Shimizu, 1991; Davidson et al., 2007; Ginibre et al., 2007; Higgins and Roberge, 2007; Jerram and Davidson, 2007; Ubide et al., 2014; Ogawa, 2018; Zellmer, 2021).

1.2 Magmatic System Framework

Grain textures along with element partitioning and diffusion behaviors as they relate to temperature, pressure, and melt composition (with or without volatiles) can be used to evaluate the petrogenetic history of a magma's crystal cargo (Ginibre et al., 2002; 2007; Blundy and Wood, 1991; Ustunisik et al., 2014; Neave and MacIennan, 2020; Jerram et al., 2018). One mineral phase that is commonly evaluated is plagioclase feldspar, thanks to its ubiquity in magmatic systems, its compositional simplicity, and the wealth of feldspar geochemical data across different systems (i.e., Grove et al., 1984; Blundy and Wood, 1991; Ginigre et al., 2007). In plagioclase feldspar for example, a temperature increase can lead to rounded habits, a decrease can lead to skeletal and acicular morphologies potentially with higher An content, while a constant temperature will create near-uniform compositions in plagioclase from core to rim (Mollo et al., 2011; Ginibre et al., 2007; Lofgren et al., 1974). Meanwhile, pressure effects are

Fig. 1: Schematic of crystal zoning patterns resulting from diverse processes operating in open systems as a result of compositional change. Autocrystic grains can preserve normal and progressive zoning, and/or resorption/dissolution due to changes in melt composition (i.e., Zellmer, 2021; Jerram et al., 2018; Davidson et al., 2007). Phenocrystic populations are expected to preserve normal compositional zoning, while xenocrystic populations can have complex histories (i.e., Zellmer, 2021). Note that physical change like decreasing pressure and depth can generate additional changes in zoning as a result of decompression-induced dissolution (i.e., dissolution of An in plagioclase feldspar, Ustunisik et al., 2014).

component will more readily resorb during decompression, which can generate reverse zoning (Blundy and Wood, 1991; Ustinusik et al., 2014). Otherwise, resorption without significant chemical change in the crystal can indicate rapid change in temperature or decompression/degassing (Ginibre et al., 2007). With respect to the coupled substitution of Ca-Al by Na-Si in plagioclase feldspar, the rate at which this occurs at subsolidus temperatures compared to exchange of other elements (i.e., Na-K) is slow enough such that An contents are likely primary in nature and not the result of diffusion (Costa and Morgan, 2011; Grove et al., 1984). Evaluation of complementary trace element abundances can help to evaluate crystal cargo petrogenesis further. For example, Sr content in plagioclase is strictly dependent on plagioclase CaO content and not pressure or temperature parameters. An increase in plagioclase Sr content from core to rim will only reflect changes in the composition of the melt due to processes like mixing, and not mechanisms like ascent (i.e., Ginibre et al. 2007, Berlo et al 2007, Bezard et al 2017; Blundy and Wood, 1991). Evaluation of rapidly-diffusing elements like MgO from core to rim in plagioclase can additionally inform recent changes in melt composition (on the order of weeks; Moore et al., 2014). While the above approaches to studying the petrogenetic history of one mineral phase have the potential to inform the evolution of the magma during the growth of that one phase, these inferences are arguably strengthened by considering additional phases within the same erupted or emplaced units whose crystallization windows may potentially combine to span the entire petrogenetic history of the magma.

In pyroxene, decompression during ascent can also trigger crystal breakdown via dissolution (Neave and MacIennan, 2020). In such a case, resorption without chemical change in the remaining portion of the crystal would be recorded, indicating either temperature disturbance or degassing/decompression (Neave and MacIennan, 2020; Streck, 2008). Interactions with hot, compositionally more primitive magmas (i.e., due to mafic recharge) can also cause dissolution in pyroxene, but could additionally be recorded by a subsequent growth zone with increased MgO and Cr content following the influx of primitive magma (Ubide and Kamber, 2018). Interaction with a magma of distinct composition could influence the compositions of new growth zones away from what would otherwise be predicted by closed-system fractional crystallization models (i.e., Lissenberg et al., 2019). An integrated approach which utilizes textural and chemical information across multiple phases has been repeatedly shown to provide new insights and constraints on the physiochemical processes that contribute to the evolution of a magmatic system's crystal cargo (e.g., Davidson et al., 2007; Jerram and Davidson, 2007; Zellmer, 2021). This type of work has been accomplished for samples originating from various tectonic settings including intraplate (Ubide et al., 2014; Couperthwaite et al. 2020; Coote and Shane, 2018), volcanic centers related to subduction zones (Velázquez Santana et al., 2020; Salisbury et al., 2008; Kent et al., 2010; Ginibre et al., 2007 and references therein), and mid-ocean ridges (Lissenberg and MacLeod, 2016; Moore et al., 2014; Bennett et al., 2019). Crystal morphologies as a result of changing conditions have most recently been summarized in Zellmer (2021) who also outlines specific terminology associated with the petrogenetic history of a crystal. This terminology is utilized throughout this work. Briefly, mineral grains that grew within their host carrier magma are referred to as autocrysts, mineral grains incorporated from distinct but petrogenetically related magmas are referred to as antecrysts, and foreign grains originating from the surrounding wall rock are referred to as xenocrysts (Fig. 1). Antecrysts can generally be identified through observation of reaction textures and unlike autocrysts, can be reversely zoned from core to rim in major and/or trace elements (i.e., Ubide et al., 2014). A grain with only reaction and/or breakdown texture but no accompanying compositional change recorded during growth from core to rim may instead record breakdown during ascent, not mixing or mingling (i.e., Neave and MacIennan, 2016).

1.3 Basaltic magmatism beyond Earth

The only direct sampling of extraterrestrial magmatic system products occurred on the Moon during the Apollo and Luna programs between 1969 and 1972 (i.e., Yang and Zhao 2018, Stooke 2017), and recently by Chang'e 5 (i.e., Qian et al., 2021). Collection of lunar meteorites found on Earth provides additional constraints on lunar magmatic system processes from a sample perspective (see Zhou 2017 and references therein). Whole rock composition analysis has been combined with remote sensing evaluation of the physical extents of lunar lava flows to further estimate magma ascent rates and viscosities, with implications for eruption and emplacement mechanisms of extraterrestrial lavas (i.e., Wilson, 2009, Gawronska et al., 2022). Over decades of study, researchers have observed several distinct geochemical differences between suites of lunar basalts. Overall, lunar basalts vary greatly with respect to their whole rock TiO_2 contents; <1 wt. % to 14 wt. %, their whole rock Al_2O_3 contents; 5 wt. % to 20 wt. %, and their whole rock K_2O contents; below detection limit to 15,000 ppm (Papike et al., 1976; Neal and Taylor, 1992; Shearer et al., 2006). These compositional ranges have been interpreted to reflect partial melting of a compositionally stratified lunar mantle characterized by vertical and lateral heterogeneities. Such heterogeneities are believed to have been established during primordial Lunar Magma Ocean (LMO) solidification, which worked to differentiate the Moon into the feldspathic crust, a K-, REEs-, and P-rich reservoir known as urKREEP beneath the lunar crust, and a stratified mantle composed of olivine and pyroxene cumulates with variable amounts of ilmenite and armalcolite (see McLeod and Gawronska, 2022, for a recent summary). Partial melting of these initially stratified, and later overturned cumulates has been proposed to generate the compositional differences in the sampled basaltic samples. However, heterogeneities in lunar basalt compositions may not be wholly representative of their source regions, but may instead reflect the introduction of antecrystic grains which has been documented on Earth (i.e., Ubide et al. 2014). It is thus imperative to investigate the crystallization histories of lunar basalts using the modern terrestrial framework to better understand whether open system magmatic processes such as mixing, mingling, or recharge once operated within lunar magmatic systems. This type of work will provide additional detailed insights regarding the degree to which such processes may have affected the final compositions of basalts sampled at the surface, and thus whether those basalts are representative of their source regions. Here, we begin to evaluate the petrogenesis of lunar magmas through an integrated mineralogical, textural, and geochemical investigation of Apollo lunar basalt samples 10057, 12038, 12043, 15085, 15556, and 70017. Through the characterization of textures and chemistries preserved in mineral grains in a diverse suite of Apollo basalts, we first evaluate whether crystal populations with distinct petrogenetic histories are preserved. Through identifying distinct crystal populations, we interpret the processes that may have contributed to sample petrogenesis (i.e., open system processes like mixing or closed system processes like convection), discuss the implications for the evolution of magmatic systems on planetary objects which lack plate tectonics, and recommend future directions.

1.4 Sample descriptions

Samples were chosen for this study based on their textural and whole rock chemical diversity (see Table S1). Samples include 10057, 12038, 12043, 15085, 15556, and 70017. Detailed descriptions of sample characteristics (textures, mineralogy), ages, and summaries of previous work can be found in Meyer (2016). Brief descriptions are provided here. Sample

10057 is a vesicular to vuggy, fine-grained (Figs. 2-3) high-Ti basalt, and is categorized as an Apollo 11 group A basalt owing to its enrichment in K and the rare earth elements (REEs, e.g., Jerde et al., 1994). This sample is hypocrystalline with a minor mesostasis/glass component (3.3-8.04% modally). Sample 12038 is an Apollo 12 medium grained, granular, low-Ti basalt with a very minor glassy mesostasis component (<1% modally). 12038 is dominated by subhedral to euhedral plagioclase feldspar laths (Fig. 2b), and has been categorized as a feldspathic basalt as a result. Sample 12043 was also collected during Apollo 12, and is classified as a low-Ti pigeonite basalt. It has a porphyritic texture with macrocrystic, zoned pyroxene grains surrounded by a feldspar/pyroxene matrix (Fig. 2c). Sample 15085 is coarse-grained (Fig. 2d), non-vesicular, holocrystalline, and equigranular basalt belonging to the low-Ti quartz-normative group collected during Apollo 15. Sample 15556 is also a low-Ti basalt and represents the olivine-normative Apollo 15 basalts. It is highly vesiculated (~49% by volume, Gawronska et al., 2022) and hypocrystalline with a minor glass component (1 %). 15556 also contains ~2% modally of

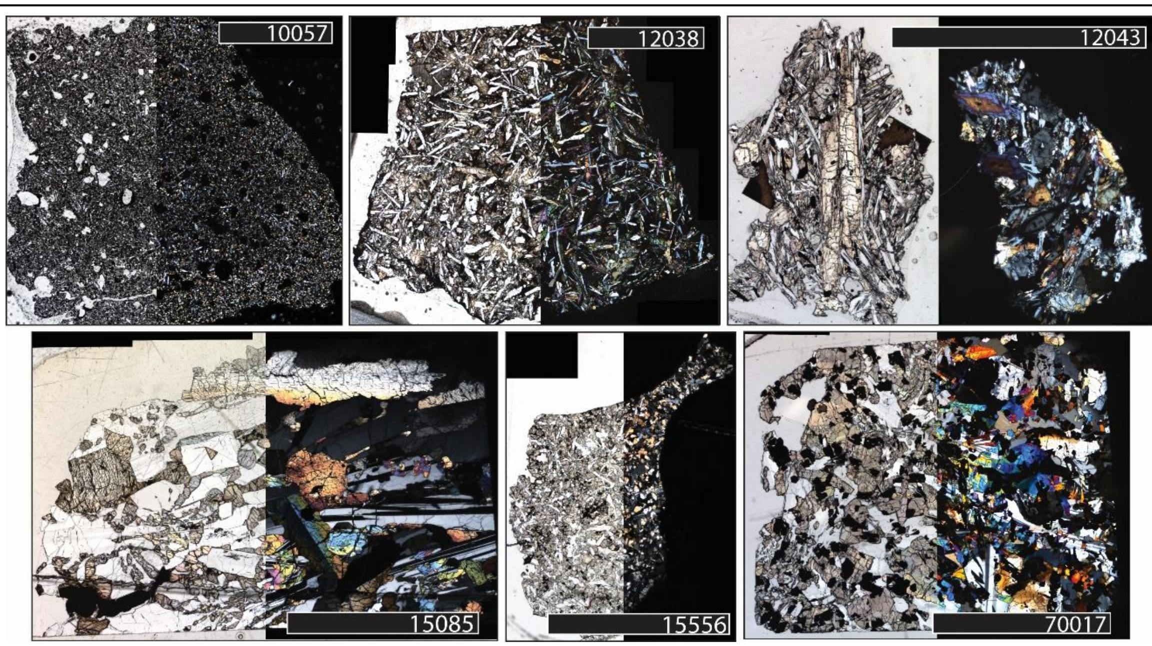

Fig. 2: Photomicrographs of representative thin sections in plane polarized light and cross polarized light for each sample. Scalebars are 5 mm.

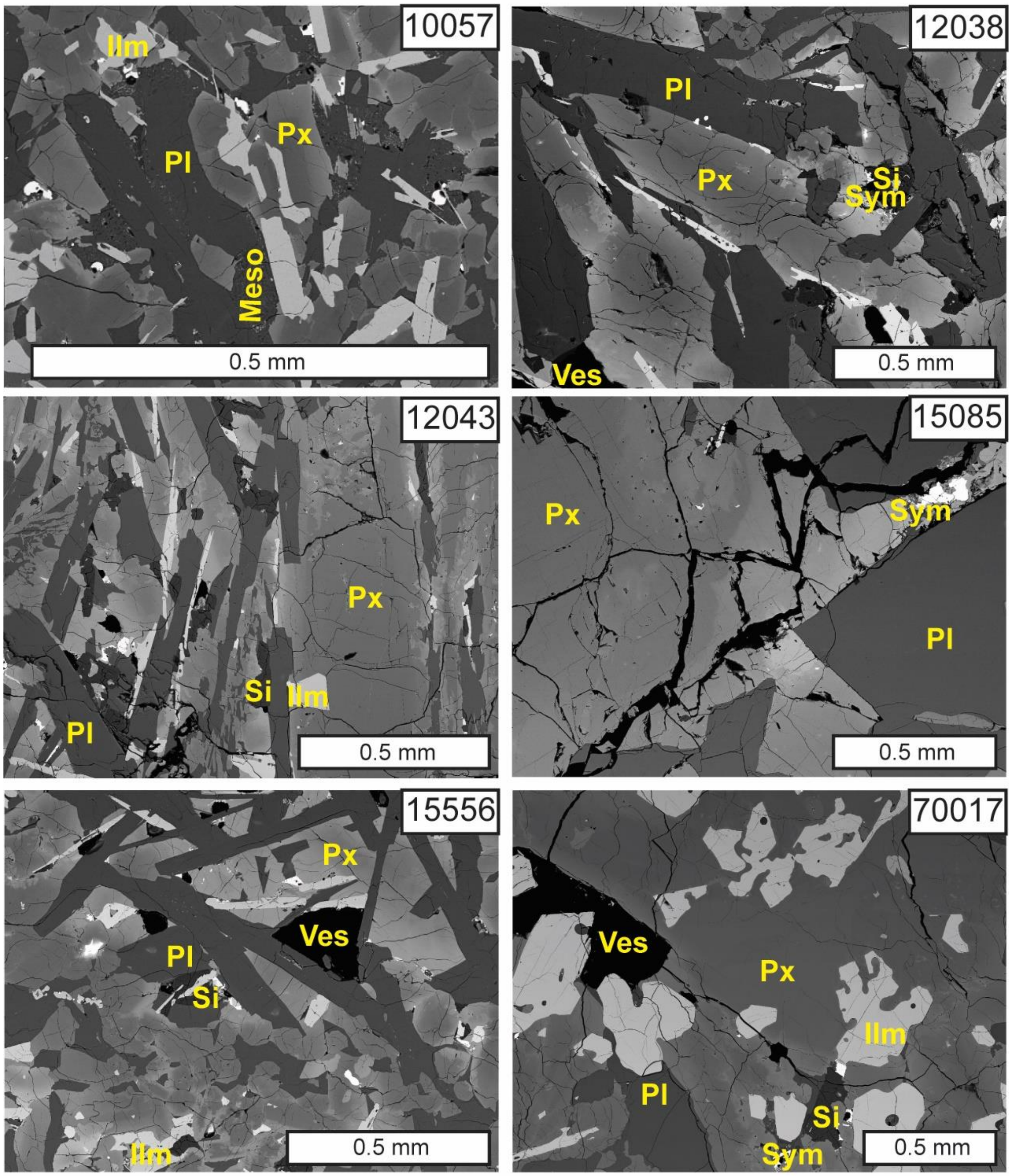

Fig. 3: Detail of sample textures imaged via SEM BSE. Annotations indicate the following components: Pl = plagioclase feldspar, Px = pyroxene, Ilm = ilmenite, Meso = mesostasis, Si = silica-rich phase, Sym = symplectites, Ves = vesicle.

macrocrystic olivines set in a fine-grained plagioclase/pyroxene matrix (Fig. 2e). Sample 70017 is a medium to coarse grained high-Ti basalt belonging to the Apollo 17 group B, and contains “chains” of ilmenite (Fig. 2f; Meyer, 2016; Paces et al., 1991).

2 Methods

2.2 Microscopy

We used light and electron microscopy to document sample mineralogy and textural characteristics. Thin sections were first characterized using a Leica DM2700 P polarizing light microscope (PLM). Additional data was collected via a Zeiss Supra 35 VP FEG Scanning Electron Microscope (SEM) in-house at the Miami University Center for Advanced Microscopy and Imaging (CAMI). Characterization via SEM involved acquisition of 1) backscatter electron (BSE) images and 2) energy dispersive X-ray spectroscopy (EDS) elemental maps. Both datasets for each sample were collected at a resolution of 2048 by 1536 pixels, a dwell time of 256 µs, a working distance of 10 mm, and an accelerating voltage of 20 keV. Individual images and maps were stitched together using *Illustrator* (Adobe Inc. ©, version 23.0.1). Finally, *ImageJ* (version 1.52a; Schneider et al., 2012) was used to merge individual elemental maps which supported an initial, qualitative, evaluation of the relationships between mineral textures and chemistries (see Figs. 3, S1).

2.3 Crystal Size Distribution Analysis

Imaging via PLM and SEM facilitated identification of phase boundaries. This spatial context permitted crystal size distribution (CSD) analyses to be undertaken in order to evaluate the crystallization history of each sample. The free software GNU Image Manipulation Program (GIMP, version 2.8.18, www.gimp.org) was used to outline each sample, followed by the outlining of individual crystals. During this process, touching crystals remained on separate layers. The outlines were filled, and layers with data were exported from GIMP as images for further analysis. In *ImageJ*, the area of the sample was extracted, along with the areas, lengths, and widths of each grain. This data was next processed through the CSD Slice 2.0 Excel spreadsheet (Morgan and Jerram, 2006), then plotted via the *CSD Corrections* program developed by Higgins (2000). *CSD Corrections* first calculated the most likely three-dimensional shape of each grain, and then determined the natural log of population densities as a function of grain long axes. This process has been documented as successfully quantifying grain cooling histories in both terrestrial and extraterrestrial sample studies (i.e., Higgins, 2000; Morgan and Jerram, 2006; Neal et al., 2015; Donohue and Neal, 2015). Phases investigated via CSD analysis included plagioclase feldspar and ilmenite. To ensure CSDs of a phase with tabular habit (i.e., plagioclase feldspar) are as accurate as possible, 200+ crystals must be outlined (Morgan and Jerram, 2006). For this reason, sample 15085 could not be investigated via CSD. Crystal frequencies are summarized in Table S2, and individual CSDs are reported in Fig. S2. As no sample contained a statistically significant number of olivine grains, olivine was not considered.

2.4 Geochemical Analysis

Next, the major element oxide (i.e., SiO_2, CaO, MgO) concentrations of the silicate phases of feldspar, pyroxene, and olivine (where available) were quantified in-situ via electron probe microanalysis (EPMA). This was accomplished on a JEOL JXA-8230 electron microprobe at Louisiana State University via energy dispersive spectrometry. In-situ analyses of trace elements in these phases followed, and were carried out via laser ablation inductively coupled plasma mass spectrometry (LA-ICP-MS) on a NWR193 laser ablation system connected to a Thermo Icap Q ICP-MS at the University of Arkansas. Data was collected as individual spot analyses to ensure that data was “spot-resolved,” i.e., the exact location and chemistry of each spot was known and there was no overlap in spots.

3 Results and Discussion

3.1 Apollo 11 high-Ti basalt 10057

Generally, pyroxene and ilmenite in 10057 are equigranular (~0.2 mm), while the feldspar grains range in size and habit from small (~0.02 to 0.2 mm) anhedral, interstitial grains to larger (~0.3 mm) subhedral/euhedral, tabular grains (Figs. 2-3). Both feldspar and ilmenite CSDs are constant, indicating that neither of these phases records a significant change that would otherwise impact crystallization rate during cooling (Fig. 4). Due to the fine-grained nature of this sample, only three plagioclase feldspar grains could be analyzed via LA-ICP-MS at both the core and rim. Considering major element chemistry, we identified one plagioclase grain that is subhedral and tabular (which is not texturally distinct with respect to other feldspar grains) with reverse zoning in An (core: An_{78}, rim: An_{87}), normal zoning in FeO (core: 0.56, rim: 0.60 wt. %), and an elevated core La/Sm ratio of 4.96, relative to other normally-zoned feldspar crystals (cores: approximately An_{82}, ~0.80 wt. % FeO, La/Sm <3.5; rims: $<An_{80}$, >0.60 wt.% FeO, La/Sm ~2.5 to 3; Fig. 5). The one reversely-zoned also has a ~40 ppm increase in Sr content from core to rim (Fig. 6). Because reverse zoning in major element content corresponds with changing Sr compositions, this grain is interpreted to record a change in its crystallization conditions during growth, likely interaction with a more primitive magma. An additional normally An-zoned crystal also records an increase in Sr at the rim. Both are depleted in other trace elements (e.g., Rb, Sr) relative to a more enriched normally-zoned grain containing elevated REE core contents (Fig. S4) and high La/Y (Fig. S5). Eu/Eu* anomalies were calculated using chondrite-normalized values (after Sun and McDonough, 1989) as Eu/Eu* = (2*Eu)/(Sm+Gd). The Eu/Eu* systematics for this sample record a decrease in Eu/Eu* from core to rim in both of the grains which record an increase in Sr (Fig. S5). The distinct relationship in

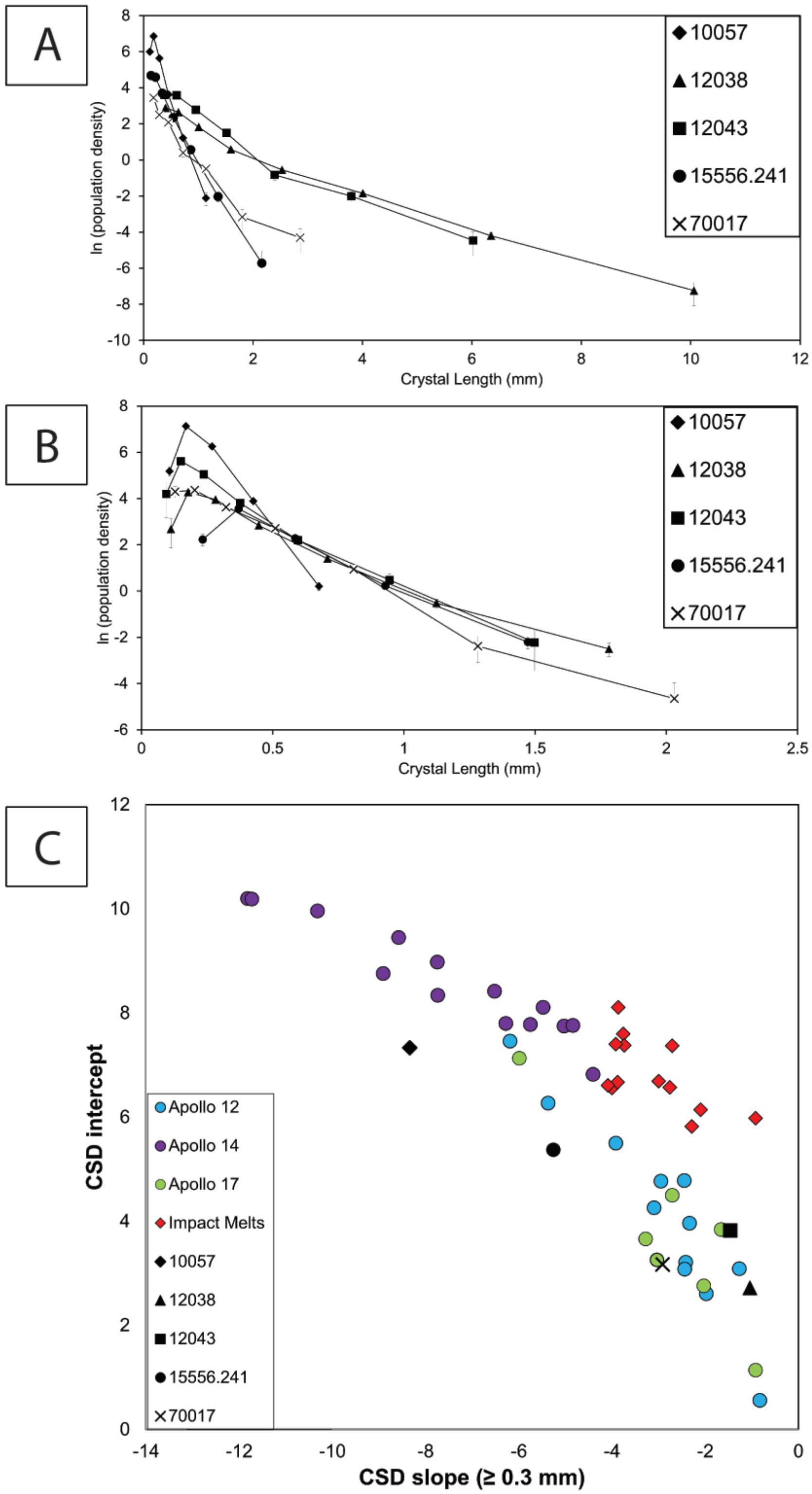

Fig. 4: A) CSDs of plagioclase feldspar in each sample; B) ilmenite CSDs for each of the samples. C) The approximate CSD intercept and slope for plagioclase feldspar in each sample plotted against data collated in Neal et al. (2015).

An vs. La/Y and An vs. Eu/Eu* between the reversely-zoned grain and the normally-zoned grains may indicate that these grains all crystallized in distinct magmatic environments. However, these grains are not texturally distinct suggesting they experienced similar cooling histories (consistent with the constant CSD), which may indicate that compositional changes are related to incorporation of material with distinct composition via a process such as mingling, which would not fully homogenize melt composition prior to crystallization. Previous work has proposed that sample 10057 experienced assimilation of KREEPy material during its petrogenesis (Jerde et al., 1994). This is supported by the abundance of K-rich mesostasis, and by approximately half of the feldspar cores analyzed here having elevated trace element contents (i.e., >16 ppm Rb, relative to <5 ppm for the remaining grains, Fig. 6; note that these grains are too small for rim analysis via LA-ICP-MS).

In the pyroxene population, one glomerocryst (Fig. S3) contains larger grains in comparison to all other pyroxene within this sample: ~0.35 mm vs. <0.2 mm long. As mentioned above there are regions of K-rich mesostasis in this sample, and pyroxenes nearby to this mesostasis preserve reaction textures (i.e., resorption). In BSE, pyroxene grains in the glomerocryst display patchy zoning which is distinct from the progressive zoning observed in other pyroxenes. In addition, glomerocrystic pyroxenes contain small ilmenite and feldspar inclusions (Fig. S3). One grain in the glomerocryst has close to constant Mg# (core: 74.1, rim: 72.2), while matrix grains range from Mg# 74.1 to 70.4 in the core and Mg# 56.5 to 17.1 in the rim (i.e., showing normal zoning; Fig. 7). Along with one other matrix grain, the grain analyzed within the glomerocryst has relatively higher CaO values in the core (~17 wt. %) relative to other, non-glomerocrystic cores (<15.5 wt. %; Fig. 7). The glomerocrystic grain is additionally depleted in the trace elements Cr, V, and Sc and elevated in REEs in its core relative to other,

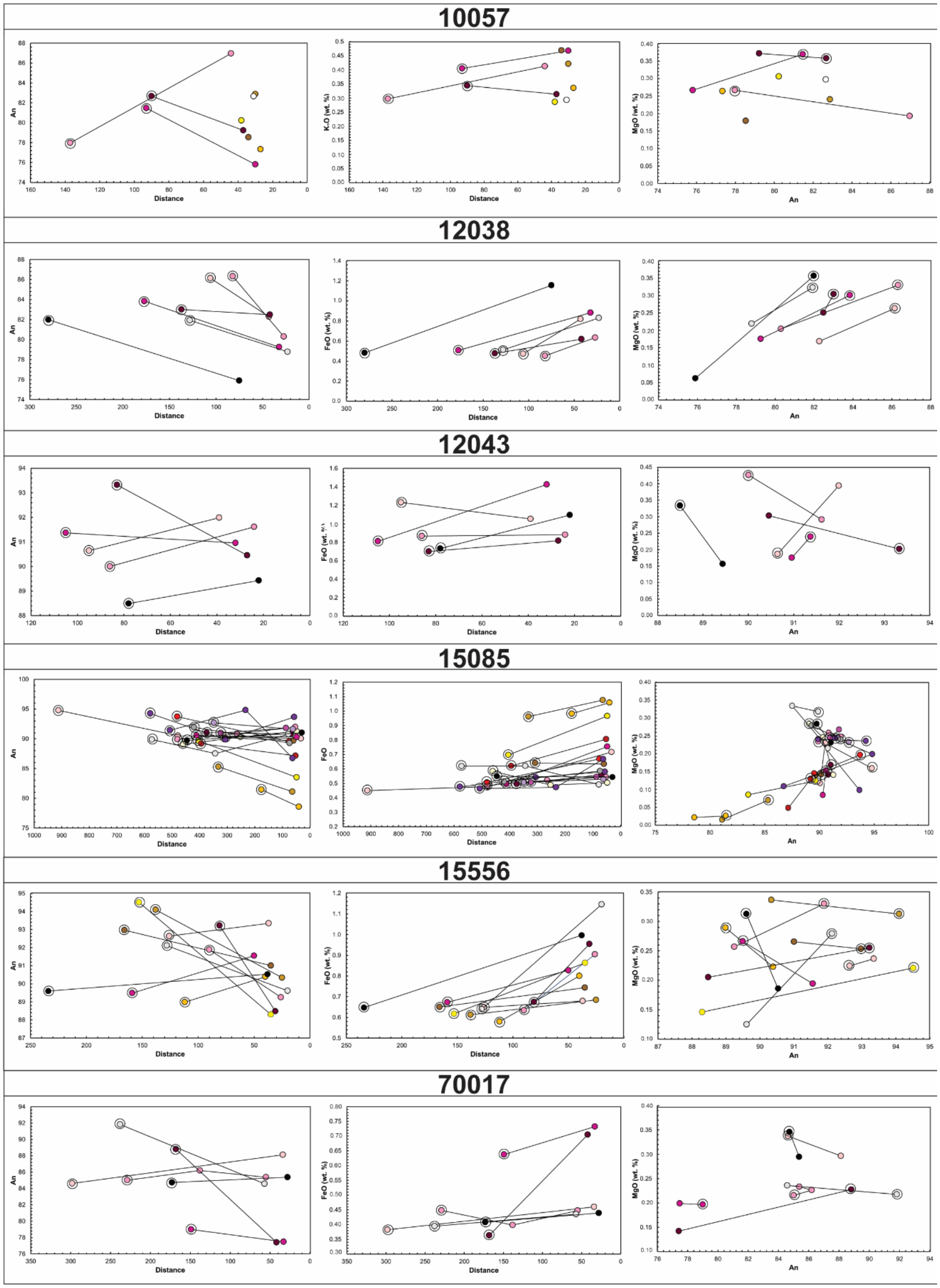

Fig. 5: Select major element data for plagioclase grains studied here. Encircled points denote crystal cores.

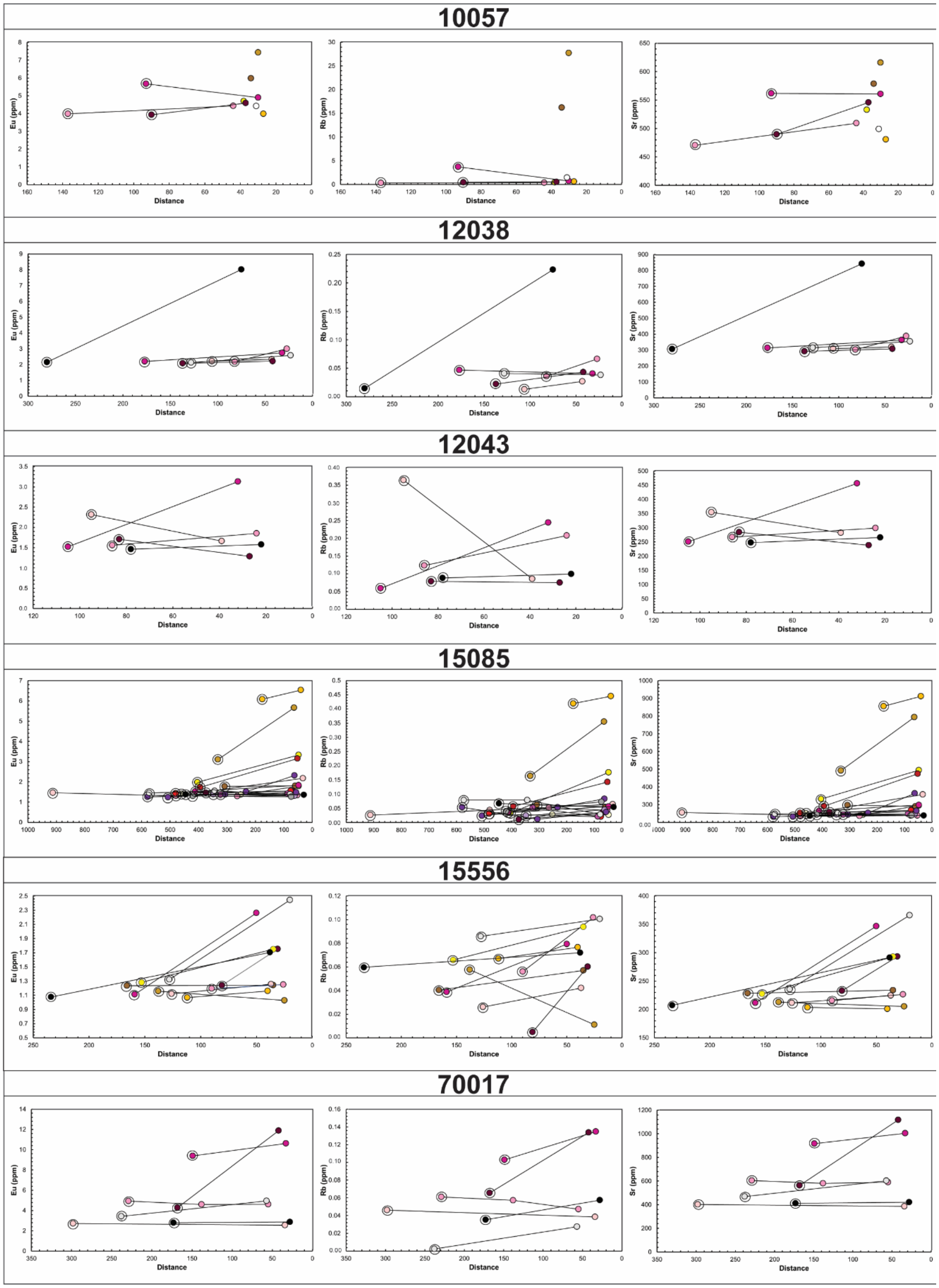

Fig. 6: Select trace element data for plagioclase grains studied here. Encircled points denote crystal cores.

non-glomerocrystic grains' cores (Figs. 8, S6-S7). Specifically, the grain within the glomerocryst is reversely zoned in Cr, which is interpreted as recording an influx of primitive magma that was able to effectively mix with the melt initially surrounding this growth, potentially due to recharge (i.e., Costa and Morgan 2011, Ubide and Kamber, 2018, Ubide et al 2019). Thus, based on its distinct texture and geochemistry, the pyroxene glomerocryst is interpreted here as being antecrystic. It is possible that this glomerocryst was plucked from a mushy lens by a hotter, more primitive melt which now represents the remainder of the sample, whereby the change in composition and temperature worked to unlock the mush (see discussion by Neave et al., 2021 and references therein). A change in melt composition due to primitive influx would also generate reverse An and Sr zoning seen in some plagioclase grains. After rising, this magma with an entrained glomerocryst and reversely-zoned feldspar is inferred to have interacted with a more KREEPy magma batch, generating pyroxene resorption and potentially generating reverse Sc-zoning of one analyzed pyroxene grain that is next to mesostasis (black in Fig. 7). This additionally may have led to incorporation of a distinct feldspar population highly enriched in REEs, and generated the K-rich mesostasis seen in this sample.

3.2 Apollo 12 feldspathic basalt 12038

In 12038, both plagioclase and pyroxene are seriate, ranging in size from 0.1 to 10 mm (Fig. 2). Feldspar grains range in habit from euhedral tabular grains to subhedral laths, and some are subophitically contained within pyroxene grains (Fig. S3). CSDs performed here record slight upward curves in both plagioclase and ilmenite (Fig. 4), indicating accumulation and/or coarsening. All feldspar grains analyzed have relatively high CaO wt. % cores (An_{82} to An_{86}), high MgO cores (0.26-0.36 wt. %), and low FeO cores (~0.5 wt. %; Fig. 5). In terms of trace elements, plagioclase cores are low in Eu (~2 ppm), and Sr (292.2 to 306.9 ppm) relative to their

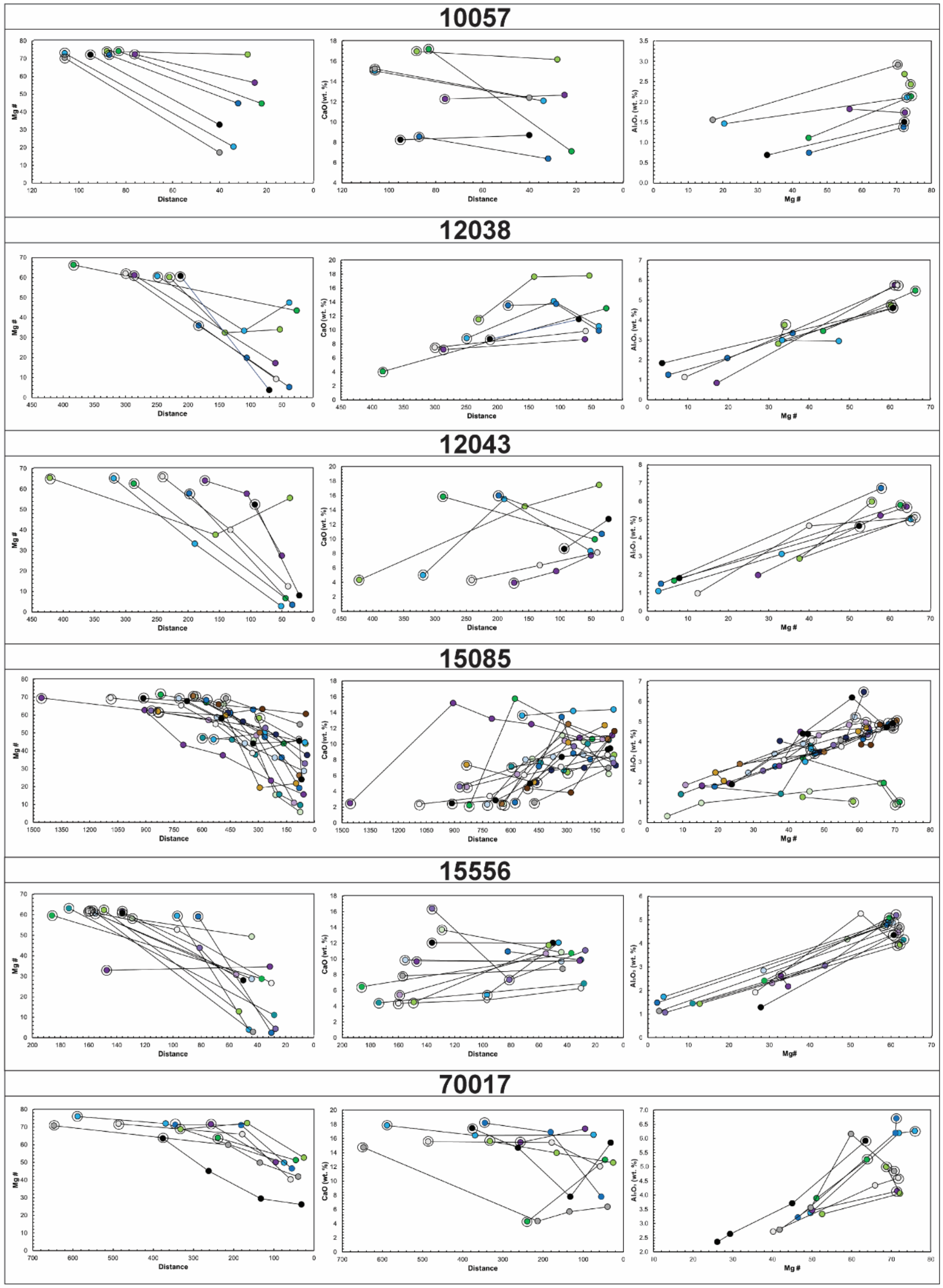

Fig. 7: Select major element data for pyroxene grains studied here. Encircled points denote crystal cores.

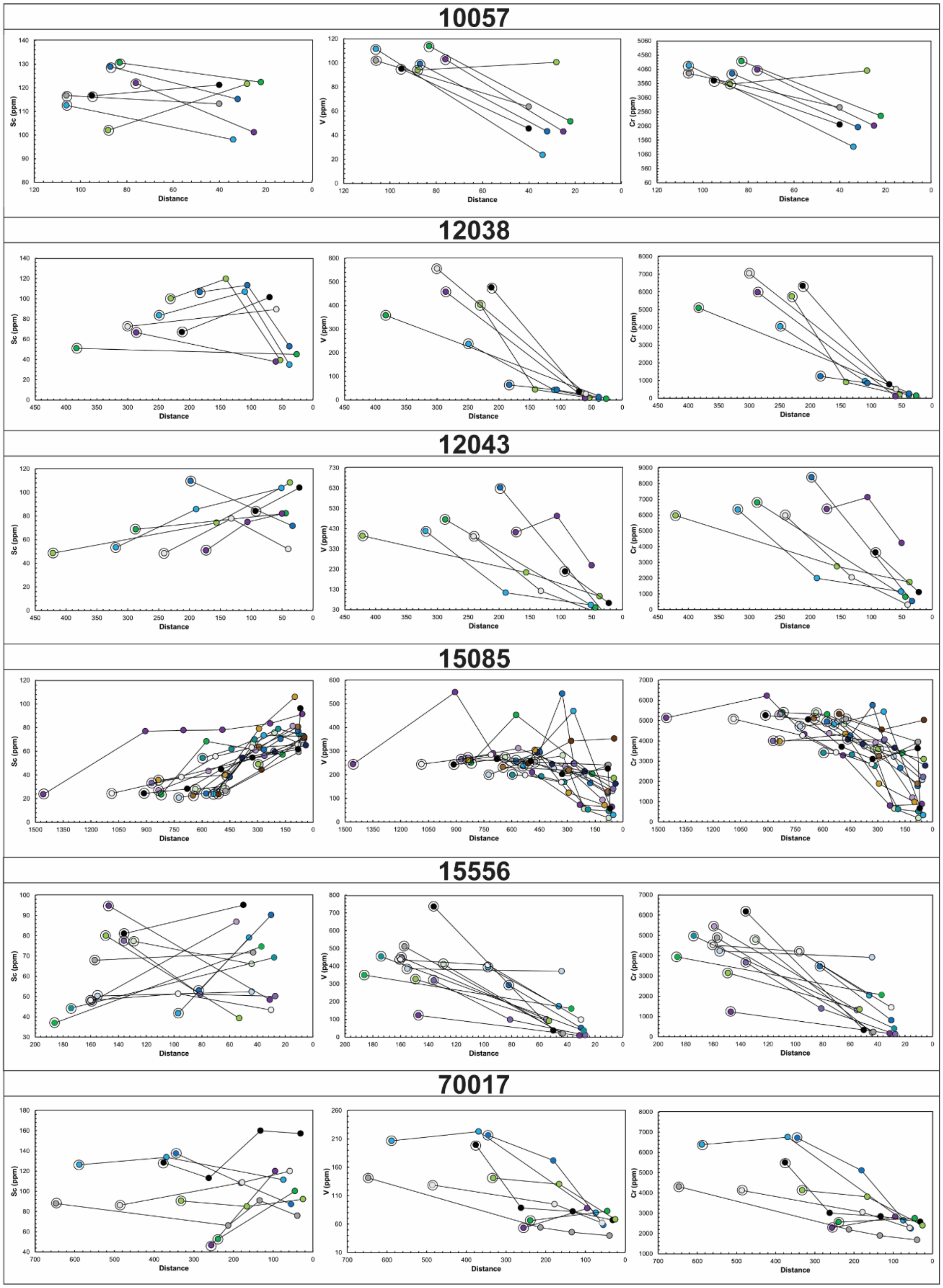

Fig. 8: Select trace element data for pyroxene grains studied here. Encircled points denote crystal cores.

respective rims, but the difference from core to rim in Eu is <1 ppm, and in Sr <100 ppm except for one subophitic grain (Figs. 6, S4-S5). Eu/Eu* anomaly values show that all grains preserve similar evolution from core to rim (Fig. S5). Because all analyzed feldspar grains record the same petrogenetic history (as indicated by similar major and trace element signatures from core to rim), geochemical signatures that would otherwise be indicative of open system processes are not evident within the plagioclase population. Crystallization of feldspar is thus inferred to have occurred under closed system conditions, with grains experiencing either accumulation or coarsening during crystallization (as evidenced by CSD work).

All pyroxene grains in 12038 are subhedral to anhedral. Some are sieved near the rim and breaking down to 3-phase symplectite (e.g., Fig. S3). All pyroxenes are normally zoned from core to a mantling zone (Fig. 7; average core: $En_{47.2}Fs_{33.1}Wo_{19.7}$, average mantle: $En_{18.6}Fs_{47.1}Wo_{34.3}$), but three out of seven analyzed grains are reversely zoned after this with higher MgO and lower CaO towards the rim ($En_{28.2}Fs_{39.7}Wo_{32.1}$, as opposed to normally-zoned rims of $En_{7.0}$ $Fs_{70.5}Wo_{22.5}$ of other crystals). One grain is additionally reversely zoned in Al_2O_3 from mantle (2.8 wt. %) to rim (3.8 wt. %) relative to other grains (rims: ≤2 wt. % Al_2O_3; Fig. 7). All grains are normally-zoned in Cr and V, but those with reverse MgO and CaO near their rim also initially increase in Sc by ~20 ppm, and then decrease again in Sc by 60-80 ppm toward the rim to match the Sc core content of a grain with the highest Mg# (52.5) found (Fig. 8). An influx of primitive magma should increase the Cr content at the rim, while mixing with another batch should distinctly affect major and trace element contents, but the element variations here are comparable within and between cores and rims (i.e., Figs. S6-S7). Thus, we conclude that the intragrain geochemical signatures are related to local differences in the melt that may have been produced by movement through a compositional gradient via a process like convection.

Pyroxene breakdown can occur from changes in pressure alone during ascent (Neave and MacIennan, 2020), which we invoke here to explain disequilibrium textures (sieving and symplectites; Fig. S3). This sample is currently the only feldspathic basalt in the Apollo 12 suite (i.e., Neal et al., 1994), and is not petrogenetically related to other Apollo 12 basalts based on REE and isotopic contents (Nyquist et al., 1981).

3.3 Apollo 12 pigeonite basalt 12043

This porphyritic sample contains pyroxene macrocrysts (1 to 5 mm) in a matrix of feldspar and pyroxene grains that, in certain locations, are radially growing out of points of common nucleation (Fig. S3). Plagioclase grains are seriate (~0.02 to 0.55 mm) and subhedral to euhedral. Some preserve quenched, skeletal textures, and all are oriented along a flow plane and pushed up against pyroxene macrocrysts (Figs. 2-3). There is a kink in the feldspar CSD suggesting a change in cooling parameters, but not in the ilmenite CSD (Fig. 4), which together indicate that a change in the cooling history of this sample may have occurred either prior to ilmenite crystallization, or that the ilmenite crystal population is not large (or abundant) enough to have recorded it. Compositionally, feldspar does not record significant changes in An content, but several feldspar grains are normally zoned from high An cores ($An_{93\text{-}91}$) to lower An rims ($An_{91\text{-}90}$), while others trend reversely from variably low An cores ($An_{91\text{-}88}$) to variably higher An rims ($An_{92\text{-}89}$; Fig. 5). One of the reversely-zoned grains is also reversely zoned in MgO from core to rim (0.19 and 0.39 wt. %, respectively) which could indicate incorporation of a grain which crystallized in a more evolved melt, as opposed to the remaining reverse-An grains which have the opposite correlation (high-MgO cores, lower MgO-rims; Fig. 5). The core of this low-MgO grain is also enriched in Rb (0.36 ppm) relative to other grains (<0.12 ppm Rb in core; Fig. 6), but otherwise is not clearly distinct. There is only limited correlation between Sr values and

An content, which may indicate that reverse An is a consequence of rapid decompression during ascent through the system as opposed to changing magma composition. However, Eu/Eu* anomaly values show the opposite relationship between reversely-An zoned and normally-An zoned grains (Fig. S5), perhaps indicating that grains grew in distinct magmatic environments prior to ascent.

Texturally, at least two populations of pyroxene are defined - the coarse-grained (>0.5 mm long), subhedral to euhedral megacrysts, and the smaller (<0.5 mm long) subhedral to anhedral matrix pyroxenes (Figs. 1-3). Most of the macrocrystic pyroxenes have sieved mantles that correspond to an increase in CaO, and are visibly zoned under polarized light (Figs. 2-3). All pyroxenes here are normally zoned, with core Mg# of >57.8, except for a matrix grain that is interpreted to record a later stage of growth (black in Fig. 7). Two analyzed macrocrysts are notably elevated in CaO in their cores (~16 wt. %), while two other grains have mantles that are elevated in CaO (~15 wt. %), but their cores are comparable to other macrocrysts (~4 wt. % core CaO). Of the two grains with high CaO cores, one is also enriched in Sc, Cr, and V (109.7 ppm, 8399.8 ppm, 631.9 ppm, respectively) relative to the cores of other pyroxenes crystals (<85 ppm Sc, <6793 ppm Cr, <476 ppm V). Meanwhile, one of the grains with a high-CaO mantle is also elevated in La/Sm in its core (1.5) relative to its rim (0.6) and to other grains (Fig. 8), and in Ce/Y (0.33 core, 0.18 rim) in its core relative to other grains (Fig. S7). This LREE-enriched grain is the largest (5 mm), tabular pyroxene macrocryst visible in Fig. 2; the high CaO grains represent two macrocrysts, while other macrocrysts plot along matrix pyroxenes.

Between the REE-rich pyroxene macrocryst, the CaO-rich macrocrysts, and matrix pyroxenes, three distinct cooling histories of pyroxene may be recorded. A rising, more primitive magma encountering a mushy lens of more evolved composition could have entrained grains with higher CaO cores, and produced Ca-rich mantles around Mg-rich cores. In this scenario, the Ca-rich cores and mantles are antecrystic, having formed in a separate crystal mush. Remaining macrocrysts are compositionally similar to matrix pyroxenes in terms of major and trace element contents, but must have formed earlier considering their larger size. Neal et al., (1994) used assimilation and fractional crystallization modeling to show that 12043, and the remaining Apollo 12 pigeonite basalts, likely assimilated crustal materials of varying compositions during their petrogenesis. This work proposed that the assimilants were likely anorthositic in composition, and may therefore have provided additional CaO for pyroxene formation, and generated plagioclase populations with distinct compositional profiles. Meanwhile, transport from depth, between lenses, and/or leading to eruption may have contributed to the observed disequilibrium textures.

3.4 Apollo 15 quartz-normative basalt 15085

The grains in this sample are too coarse (average grain size of 1 to 5 mm) to attempt a CSD on any mineral phase. Feldspar grains are generally subhedral and interstitial (Figs. 2-3). Approximately one in ten plagioclase grains in this sample are concentrically zoned under polarized light (Fig. 2). Compositionally, cores of feldspar grains have highly variable An ranging between An_{92} and An_{80}. The majority of the analyzed grains decrease by 2-3 An mol% from core to rim and are thus normally zoned. However, some also display reverse zoning where An increases by 1 to 2 mol from core to rim, while four out of the 18 analyzed grains record no change in An from core to rim (Fig. 5). The normally-zoned grains range in habit from euhedral to anhedral and contain numerous small (<0.5 mm) pyroxene inclusions. The reversely zoned crystals are euhedral to subhedral, relatively large (~3.5 to 4 mm), and typically contain fewer pyroxene inclusions. The MgO contents of cores of normally-zoned An grains are relatively depleted (<0.17 wt. %) when compared to the reversely-zoned population (>0.23 wt. % MgO). In addition, the normally-zoned population records an increase in Sr at the rim (by 50 to 150 ppm) which would be consistent with the introduction of compositionally more primitive magma. This is not observed in the reversely-zoned grains or the no-change grains, neither of which record any change in Sr from core to rim indicating their An change probably comes from Na-Si dissolution during decompression (Ustunisik et al., 2014). As cooling progressed, a final late-stage interstitial population rich in Eu, Rb, Sr, and low in An formed: this additional population of feldspar grains is euhedral to subhedral, low in An (< An_{85}), high in $NaO+K_2O$ (>1.5 wt. %), Eu (>3 ppm), Rb (>0.15 ppm), and Sr (>492 ppm) in their cores relative to the remaining grains (≤ 1 wt. % $NaO+K_2O$, <2 ppm Eu, <0.1 ppm Rb, <300 ppm Sr; see Fig. 6). Thus, this population is interpreted to represent a late stage of growth.. These three feldspar populations have similar trace element, and particularly REE, contents (Figs. S4-S5) suggesting that they did not form in significantly distinct magmatic environments. Eu/Eu* systematics show a complex history of feldspar crystallization, with grains of similar An content having opposite Eu/Eu* values, i.e., some with elevated Eu anomaly values (>60) in their cores relative to their rims, and with others having lower Eu anomaly values in their cores relative to their rims (<40; Fig. S5); the late stage population is distinct on the basis of An values, but not Eu/Eu* values.

Texturally, there are at least three pyroxene populations in sample 15085. The first displays prominent sieve textures which are also associated with discrete compositional zones (Figs. 2-3; Fig. S3). At the rims of these grain, Fs-Fa-SiO_2 symplectites are also present (and, in extreme cases the pyroxenes have been completely replaced by symplectite, Fig. S3). The second population is characterized by resorbed cores, sieved textures between compositional zones, and displays only minor breakdown to Fs-Fa-Si symplectites. The third population is typically interstitial in nature and comparatively exhibits minimal sieve textures, and no breakdown to symplectite. Generally, pyroxenes in greater textural disequilibrium in 15085 have resorbed MgO- and Cr-rich cores overgrown by Ca-rich mantles, with Fe-rich rims – the transitions between each zone are sieved, and Fe-rich rims are commonly dominated by symplectite. As shown in Fig. 8, the grain mantles coincide with a 9 to 16 wt. % increase in CaO, a 3 wt. % decrease in FeO (Figs. 3,7), and a ~1000 ppm increase in Cr, 45 ppm increase in Sc, and 300 ppm increase in V (Fig. 8). One grain that is texturally similar to the first population (significantly resorbed and has been completely replaced by symplectites at the rim) is compositionally distinct, showing no significant change from core to rim in MgO, and having a core elevated in CaO (~14 wt. %) relative to the remaining cores (<7.5 wt. % CaO), and a mantle elevated in Cr (5432.7 ppm) relative to its core (4802.9 ppm). This grain is not otherwise distinct in trace elements (Fig. 8), but may also preserve evidence of sector zoning which has been partly destroyed by breakdown (Fig. S3).

From La/Sm vs/ Dy/Yb systematics (Fig. 8), there may be potentially three distinct compositions of cores which are not as clearly reflected in other compositional plots. The euhedral to subhedral grains in greatest textural disequilibrium (sieved, with occasional symplectite rims) and the highest core Mg# (>65) and Cr (>4500 ppm) with CaO-rich mantles have generally low La/Sm and Dy/Yb relative to other grains (<0.5, <1, respectively). The CaO-elevated grain described above is associated with this population despite its distinct CaO content. We conclude that this texturally and compositionally distinct pyroxene population represents a relatively early-formed, primitive, antecrystic population within sample 15085, based on definitions by Edmonds et al. (2019) and Zellmer (2021). The second population of resorbing, anhedral grains, some of which have relatively low Al_2O_3 (~1 wt. %) and high Sc (~50 ppm) compared to other populations' cores (>~3 wt. % Al_2O_3 and <40 ppm Sc), have high Dy/Yb (>1) – this may represent crystallization from a chemically distinct, more evolved melt composition. The third group of grains with less extensive sieving have lower Mg# cores (~50), lower Cr (~4000 pm), and higher La/Sm (>0.5) and Ce/Y (Figs. 7-8, S7) values. These are interpreted to represent a later stage of formation based on elevated trace and REE contents in their cores, or may be entirely distinct considering their high Ce/Y values. Moreover, this may be the only population of pyroxenes in 15085 that is in equilibrium with the final carrier magma given the lack of significant sieving or symplectite development.

For 15085 pyroxenes, primitive, early-formed MgO- and Cr-rich cores are interpreted to have been transported to a mushy lens where a compositionally more evolved interstitial melt was present. In this environment, they experienced resorption and subsequently grew CaO-rich mantles, while CaO-rich material (including the CaO-rich core found here) was incorporated. This interstitial, incorporated material was likely not significantly distinct in composition since trace element contents between these two core populations (one CaO-poor, the other CaO-rich) are similar (both with ~250 ppm V, ~23 ppm Sc, ~5000 ppm Cr, La/Sm close to 0). As crystallization continued in this magmatic environment, the interstitial melt would have become more incompatible trace element-enriched (differentiated) as a result of continued crystallization, perhaps generating the final population with elevated La/Sm and Ce/Y core signatures. These textural and chemical observations are consistent with the conclusions of Vetter et al. (1988) who determined that the Apollo 15 quartz-normative suite which this sample belongs to formed by extensive fractional crystallization of pigeonite, which are now found as phenocrysts throughout the QNB suite; their phenocrystic, early-fractionated pigeonites may be represented here as the early-forming, antecrystic population. Lindstrom and Haskin (1978) additionally argued that mixing of separate magma batches is required to produce the QNB samples, which would account for pyroxene grains with elevated La/Sm and Ce/Y ratios, and plagioclase feldspar grains with distinct Eu/Eu* vs. An relationships. A few pyroxenes in the second (in moderate textural disequilibrium) and third (in minimal textural disequilibrium) populations described here also record an increase in Cr (by 100 to 500 ppm) at the rim, which may correspond to influx of hot primitive magma that would mix with trace element-enriched interstitial melt and unlock and mobilize this cargo. These processes are discussed further in **Section 4**.

3.5 Apollo 15 olivine-normative basalt 15556

CSDs of plagioclase record an upwards curve in sample 15556,28 but no change in sample 15556,241. While ilmenite CSDs show a kink in 15556,28, no change is recorded in 15556,241 (Figs. 4, S2). This indicates a potentially complex crystallization history that is not completely recorded by the textural characteristics of these phases. Plagioclase grains are generally equigranular (~0.25 mm), range from subhedral to anhedral, interstitial, and occasionally poikilitically enclose some of the smallest pyroxene grains in this sample (Figs. 3, S3). It is noted here however that some larger feldspar grains (up to 1 mm) do exist in texturally distinct crystal clots throughout this sample (Fig. S3). Some feldspar grains display normal zonation patterns with relatively high An (>An_{91}) and low Na_2O+K_2O (most <0.8 wt. %) cores that decrease by ~2 An and increase by up to 0.5 wt. % Na_2O+K_2O towards the rim, while other feldspar grains record slight reverse zoning from lower-An (generally <An_{90}), higher Na_2O+K_2O (~1.2 wt. %) cores that record a 0.5 An increase and decrease of ~0.3 wt. % Na_2O+K_2O toward the rim. The reverse grains are anhedral, and the normally zoned grains subhedral. All grains increase in FeO from core to rim by 0.1 to 1.5 wt. %. Three out of seven normally An-zoned grains, and two of the four reversely An-zoned grains studied here, increase in Sr (by >60 ppm) and Eu (by 0.5 to 2 ppm) from core to rim. Three out of four reversely An-zoned grains also correspond to an increase in Sr from core to rim, which could indicate an influx of new, compositionally primitive magma. However, changes in the major and trace element contents across all studied grains are small; all grains display similar MgO and FeO systematics, and REE contents are consistent between grains (Figs. S4-S5), thus if any influx of new material into the crystallization environment did occur, it likely had a similar composition. Eu/Eu* anomaly values for plagioclase preserve a range of compositional changes from core to rim, with some grains recording a decrease in Eu/Eu* with decreasing An, some increase in Eu/Eu* with decreasing An, some increase in Eu/Eu* with increasing An, and one showing a decrease in Eu/Eu* with increasing An content. The complex compositional relationships in grains studied here do not correspond to textural differences, but all occur within cm of each other (within this one sample), indicating that melt composition also differed on a small scale. Local differences in the bulk rock composition of 15556 have been attributed to short range unmixing (described further below; Lindstrom and Haskin, 1978).

Pyroxenes are generally euhedral to subhedral, and seriate (0.2 to 0.5 mm long). With the exception of one grain, all analyzed grains (n=13) are normally zoned from cores with Mg# of 62 to 63 and rims of approximately either Mg# 30 or Mg# 13. There is one grain that is interstitial to feldspar, and differs from others with a lower core Mg# (32.9) and higher rim Mg# (34.7, Fig. 7). The core of this grain also has relatively elevated Sc (94.8 ppm), and lower V (122.1 ppm) and Cr (1232.4 ppm) compared to other grain's cores (<81 ppm Sc, >319 ppm V, >3140.4 ppm Cr, Fig. 8). From Sc contents, two groups of pyroxene grains are defined, where several grains are normally zoned from >75 ppm in the cores, to <66 ppm in the rims. The remaining grains (including the low core Mg# grain) have <53 ppm Sc cores and to up to 90 ppm Sc rims (Fig. 8). Grains with relatively low Sc are generally also low in REE contents (Fig. S6), while those with high core Sc have elevated REE contents, with one grain exhibiting a particularly high Ce/Y (Fig. S7). The low-Sc cores also generally correspond to low Dy/Yb core values of ~1.2, while the high Sc cores generally have higher Dy/Yb values of ~2, with some displaying high La/Sm value (>0.4, Fig. S8). Grains that are in textural equilibrium, and grains that are in textural disequilibrium (i.e., lightly sieved and resorbing) exist in both compositional populations (as defined by Sc; see Figs. 2-3, S2). As the name of the sample suite to which 15556 belongs to implies, the compositions of olivine-normative basalts are controlled by olivine growth and fractionation (Ryder and Schuraytz, 2001). Ryder and Schuraytz (2001) found that the within the olivine-normative Apollo 15 basalt suite, sample bulk compositions can vary on a mm- to cm-scale as a result of the addition or removal of olivine. For example, Sc is generally incompatible in olivine (i.e., K_D<0.5, Beattie, 1994) but generally compatible in pyroxene (i.e., K_D>1.0, Hart and Dunn, 1993), thus initial growth and fractionation of olivine would relatively concentrate remaining melt in Sc. Based on the work done here, grain Sc contents are likely related to their proximity to late-stage mesostasis. Grains with elevated Sc contents are not near mesostasis, indicating that they may have formed early when melt remained Sc-enriched following olivine fractionation; grains with low Sc contents generally border mesostasis on at least one side, indicating that they may have crystallized later on. Because core Sc contents form two distinct groups rather than a progressive change, it is possible that pyroxenes crystallized in two-stages, or from a melt that had not efficiently mixed following depletion in Sc as a result of olivine fractionation, likely due to high degrees of undercooling (consistent with plagioclase results). A melt not having effectively homogenized following fractional crystallization is consistent with previous work: Lindstrom and Haskin (1978) determined that compositional changes in the Apollo 15 olivine normative suite resulted from short-range unmixing, where early-formed phases that effectively change the composition of the remaining melt do not effectively fractionate from the melt, thus retaining early-formed grain populations alongside later-formed populations of distinct composition. High degrees of undercooling consistent with this sample's fine-grained nature may have further contributed to preclude efficient element diffusion through melt following olivine fractionation (i.e., Lofgren et al., 1974, Vernon 2018).

Sample 15556 contains olivine macrocrysts, which are skeletal at their rims (as evidenced by incomplete filling between corner growths, Figs. 3, S3), and embayed (as evidenced by irregular crystal faces, Figs. 3, S3). The olivines are normally zoned, some host melt inclusions, but none preserve resorption textures like those observed in pyroxene. The cores of olivine in 15556 are all compositionally strikingly similar, but there are two compositionally distinct rim compositions. Cores are defined by Mg# >57.5, 0.47 to 0.26 wt. % Cr_2O_3, and 0.046 to 0.27 wt. % NiO. One rim population is characterized by elevated Cr_2O_3 (0.27 to 0.35 wt. %) with no significant change in MnO or CaO toward the rim (Fig. S8). The second population records normal zoning in Cr_2O_3 to rim compositions of <0.12 wt. %, but increases in CaO (from ~0.2 wt. % in the core to >0.3 wt. %), MnO (~0.33 wt. % in the core to >0.5 wt. % in the rim).

3.6 Apollo 17 high-Ti basalt 70017

Plagioclase grains in 70017 poikilitically enclose small pyroxene, ilmenite, and olivine grains, and are generally subhedral, ranging from ~0.1 to 2 mm long. From CSDs, ilmenite records a distinct kink (Figs. 4, S2), while the plagioclase feldspar CSD is more complex, recording either multiple kinks in the distribution corresponding to a rapid change in the system, or recording one upwards curve corresponding to crystal accumulation (Fig. 4; i.e., Donohue and

Neal, 2015). Compositionally, several grains are variably normally zoned, decreasing by 1 to 5 An mol from core to rim; other grains increase only minimally by ~1 An mol from core to rim (Fig. 5). One normal zoned grain has a compositionally distinct core which is notably low in An (An_{79}) and high in FeO_{total} (0.64 wt. %) relative to other cores (>An_{84} ; <0.45 wt. % FeO_{total}), and likely formed at a later stage, as it is also elevated in total REEs (Fig. S4). Two other grains that are reversely zoned in An are elevated in MgO content (>0.3 wt. % at the core and rim) and alkalis (>1.5 wt. % Na_2O+K_2O in the core) relative to others (<0.25 wt. % MgO in cores and rims; <1.5 wt. % Na_2O+K_2O in cores). With respect to trace elements, the normally-An zoned population is also reversely zoned in compatible Eu and Sr (Fig. 6), though in varying amounts (Fig. 6), while the reversely zoned group preserves only minimal change in Eu or Sr content (<0.5 ppm Eu and <30 ppm Sr change from core to rim; Fig. 6). Some grains that are reversely zoned in An and some that are normally zoned in An show an increase in Eu/Eu* from core to rim, while other reversely-zoned grains and normally-zoned grains show a decreasing Eu/Eu* anomaly from core to rim; neither relationship is related to a particular texture. The reverse An zoning is therefore interpreted as a decompression feature (i.e., Ustunisik et al., 2014) rather than significantly changing magma composition (consistent with the lack of a kink in feldspar CSD analysis). While all feldspar grains in this sample are subhedral, the reversely-zoned grains are generally larger (>1.0 mm long) than the normally zoned populations group (<1.0 mm). Due to their larger size, higher MgO content, and decompression features, these grains likely formed earlier and a greater depth in the system. Their REE contents are however not distinct from the normally zoned population (Figs. S4-S5), thus they may reflect crystallization from partial melting of the same source reservoir.

Pyroxenes in 70017 are subhedral and poikilitically enclose most of the ilmenite present (Figs. 2-3). Based on dihedral angles, it appears that pyroxenes could have experienced textural coarsening (Higgins 2011), which is consistent with recent work by Gawronska et al. (2022). Pyroxene zoning is concentric in smaller crystals (<1 mm), but tends to be patchy in the largest grains (>1 mm; Fig. 2). Pyroxenes have cores relatively high in MgO (Mg# > ~63.5), then mantles/overgrowths with ~1 to 3 wt.% increase in MgO and ~400 ppm increase in Cr, and final Fe-rich rims (Mg# <53). Those mantling zones and patches often correspond to sieve textures (Figs. 1-3, S2). From textural and compositional observations three populations of pyroxene may be present. One population is relatively primitive in composition with elevated Al_2O_3 (>5.9 wt. %), Sc (>120 ppm), V (>200 ppm), Cr (>6000 ppm) in their cores relative to other populations and is interpreted as having formed before plagioclase. This population is represented by the largest (> ~1.5 mm) pyroxene grains that record both progressive and patchy zoning. A second population is compositionally more evolved. Grain cores are depleted in CaO (<5 wt. %), Sc (<55 ppm), V (<70 ppm), Cr (<3000 ppm), and exhibit lower Dy/Yb values (~1), relative to other cores (Figs. 7-8). This population is made up of the smallest (generally <0.5 mm), euhedral, concentrically zoned crystals. A third population is defined by compositions between these two populations (Figs. 7-8), ranging in size from 1.5 mm to 0.5 mm, and generally recording patchy zoning. Because mantling zones of the first population of grains are in textural disequilibrium, these grains likely represent stages of growth in distinct environments. Three stages of pyroxene growth at different storage locations in the magmatic system are probably represented, which is consistent with select plagioclase grains showing storage at depth prior to ascent (as revealed by reverse An zoning that is not coupled with changing plagioclase Sr content). Resorbed cores of the largest pyroxenes are interpreted as older and antecrystic, eventually being transported by more primitive melt (which imparted sieved mantles that are slightly elevated in MgO, Cr; Figs. 7-8) to a new location where a compositionally more evolved population grew. Evolved, small pyroxenes would represent a population that originate from this lens. Interestingly, the small evolved pyroxenes are reversely zoned in Sc and have distinct core Ce/Y values (Fig. S7), and may thus represent a wholly distinct magma batch that was encountered by a more primitive melt rising with the larger primitive pyroxenes. Prolonged storage in any melt lens, at any stage, may explain the textural coarsening seen documented here and discussed in Gawronska et al. (2022).

Three olivines were analyzed in this sample – two have core Mg# of ~67, Cr_2O_3 <0.2 wt. %, MnO of 0.3 wt. %, while the third has core Mg# of 52.7 wt. %, but Cr_2O_3 of 0.26 wt. %, and MnO of 0.4 wt. %. If interpretations from feldspar and pyroxene elemental stratigraphies are correct, then this third olivine grain may have formed after the proposed two magma batches came in contact.

4 Implications for Lunar Magmatic Systems

As documented by the pyroxene and feldspar crystal populations throughout the samples studied here, the Apollo mare basalt crystal cargoes record evidence (Fig. 1) of interactions between materials of distinct compositions at various stages of fractionation. Specifically, samples 10057, 12043, 15085, and 70017 clearly indicate that grains which initially crystallized in compositionally more primitive magmatic environments now coexist with grains that grew in relatively more compositionally differentiated melts. By definition, these types of interactions can only happen in a so-called “open” magmatic system, i.e., one where material can be exchanged through a variety of processes (i.e., Davidson et al., 2007; Ginibre et al., 2007; Jerram and Davidson, 2007; Ubide et al., 2014; Ogawa, 2018; Zellmer, 2021). Thus, it is established that the petrogenesis of at least some lunar basalts is associated with open system processes. Furthermore, magma differentiation likely occurred in distinct lenses within the lunar crust where magma batches were later remobilized and mixed prior to eventual emplacement on the lunar surface. This work suggests that plumbing system architecture evolves similarly across rocky planetary bodies, and may operate similarly on other bodies where magmatism has operated previously or currently operates, including Mars, Venus, and Jupiter's moon Io (Wilson 2009, and references therein). Below, we outline the major implications this has for our understanding of magmatic systems on the Moon.

4.1 Evaluating the potential role of crystal mushes

On Earth, it has been recently recognized that magmatic systems exist as a combination of mushy lenses which can collectively extend vertically throughout the crust (Cashman et al., 2017; Sparks et al., 2019). These so-called "mushes" are continuous networks of crystals through which melt is distributed, and in which rheological properties are controlled by the crystalline network as opposed to magmas, whose rheology is controlled by melt (Cashman et al., 2017; Sparks et al., 2019). The transition between these two domains occurs approximately at 30 to 50% remaining melt (Sparks et al., 2019). Mushes form as magmas incrementally intrude into the crust, pond in lenses, and solidify over time to form crystal-rich networks (i.e., Sparks et al., 2019). Mush crystal frameworks are likely variable in modal proportion and vary on a centimeter to meter scale (i.e., Lissenberg et al., 2019). The igneous crystal cargoes produced throughout these mushy lenses, at any given stage, will crystallize and texturally and chemically trace their magmatic environment(s). Because magmatic systems stored as a network of mushy lenses can be extensive, some crystal populations may form early on (i.e., at depth) in a system's history and later rise (ascend) towards the surface in a carrier magma of distinct composition. Being out of equilibrium with carrier magma, and having crystallization from a chemically distinct source, defines antecrysts (Zellmer 2021). Due to the nature of differentiation and distance from mantle source reservoir, lenses which exist deeper within the crust are more likely to be primitive in composition, while upper lenses are more likely to be characterized by more evolved compositions (Cashman et al., 2017; Jackson et al., 2018). Within this framework, there are plagioclase grains in 10057, 12043, 15085, and 70017 that may be antecrystic in nature based on their more primitive compositions. Furthermore, their decompression features suggest initial growth occurred at depth. Meanwhile, the pyroxene glomerocryst in 10057, pyroxene macrocrysts in 12043, 15085, and 70017 are also antecrysts as evidenced by their disequilibrium textures. This includes resorption in conjunction with changing crystal compositions which likely corresponds to changing melt compositions as a result of mixing between mush melt and intruding primary melts (Fig. 1). Thus, the crystal cargoes from four of six mare basalt samples studied here clearly indicate that lunar magma plumbing systems are similar in architecture to some of their terrestrial counterparts.

4.2 Melt Transport Through and From a (Mare) Mush

If lunar magmatic systems operated through a network of mushes, melt transport mechanisms must also be further evaluated. In a melt-dominated system, melts can propagate upwards through a network of dikes and sills (i.e., Lissenberg et al., 2019; Wilding et al., 2023). On the Moon, melt transport may additionally be supported by crustal fracturing as a result of bombardment (Whitford-Stark, 1982). In a system where connected chambers are dominated by mush, it is predicted that melts will migrate through the mush by porous flow over time (McKenzie, 1984; Sparks et al., 2019). As crystallization progresses, the melt will either segregate to generate a secondary, separate eruptible melt lens (or chamber), or will become compacted, and will concentrate into highly porous melt layers within the chamber (Solano et al., 2014). The buoyant melt layers may then escape upwards due to their buoyancy and establish new lenses at shallower levels, or erupt (i.e., Lissenberg et al., 2019; McKenzie 1984; Solano et al., 2014; Sparks et al., 2019). Besides porous flow, on Earth melts within magmatic systems are also known to be displaced by flow focused in a conduit through a mush. This process is comparatively more rapid (i.e., Lissenberg et al., 2019; Richter and McKenzie, 1984). This displaced flow may eventually reach the surface during an eruption, which occurs due to remobilization of otherwise immobile, solidified components (Sparks et al., 2019). Eruption of crystal-containing melt at the surface can be aided by remobilization of materials through heat, potentially as a result of an intrusion at depth or the influx of a hotter, more mafic magma into a storage region. This occurs during mafic recharge and is commonly invoked as a cause for eruptions on Earth (Huber et al., 2011, Lissenberg and MacLeod, 2016; Sparks et al., 2019; Ubide and Kamber., 2018). In particular, eruptions appear to be common in relatively small systems following recharge, though relatively larger systems may be more buffered against this (Ginibre et al., 2007). The intrusion of hot, primitive magma at depth within a magmatic systems has been shown to be effective at fluidizing crystal mushes, allowing them to rapidly ascend in crystal-poor “chimneys” (Schleicher and Bergantz, 2017; Spera and Bohrson, 2018; Bergantz et al., 2015).

4.2.1 Porous Flow of Melt in Mush

As a magma lens continues to evolve and establish a crystal framework, the remaining interstitial melt will become compositionally evolved, and in disequilibrium with grains in the network (Lissenberg et al., 2019). Because of this, recent work on terrestrial magmatic systems at mid-ocean ridge settings suggests that melt coexisting with a mush becomes reactive (Solano et al., 2014; Lissenberg and MacLeod, 2016; Lissenberg et al., 2019) and moves through the mush via reactive porous flow (RPF). Based on compositional modeling of melts at mid-ocean ridge settings, reactive melts can range in composition from primitive (basaltic) to evolved (dacitic) and can thus lead to various interactions with grains in the mush (see discussion by Lissenberg and MacLeod, 2016). Interstitial melts can also become remobilized and mix with any replenishing melt entering the system via a process like recharge. This leads to the possibility of two reactions: one between the mush framework and the increasingly evolved interstitial melt, and one between the mush framework and any hot, primitive, replenishing magma entering the system (Lissenberg et al., 2019; Lissenberg and MacLeod 2016). Such interactions cause crystals within the mush to develop dissolution fronts, ragged grain boundaries, symplectites, and compositions distinct from those otherwise predicted by fractional crystallization models, particularly in terms of trace element contents (i.e., Lissenberg and MacLeod, 2016). The large variety of disequilibrium features observed in terrestrial magmas as a result of RPF are reminiscent of the high degree of textural equilibrium observed in the 15085 pyroxenes (Figs. 3, S3). Pyroxenes in this sample record resorption and in some cases complete breakdown to symplectites. It is however noted here that the 15085 symplectites are defined by ferrosilite, fayalite, and an Si-rich phase, which is different to the clinopyroxene-amphibole symplectites assemblages observed in terrestrial mid-ocean ridge basalts in which RPF studies have primarily been completed (see Lissenberg et al., 2019, and references therein for more information). Resorption, breakdown, and ragged grain boundaries are also seen in pyroxenes in 70017, and to a lesser degree in 12043. At the time of writing, RPF is not a completely understood process in terrestrial systems but it does appear to be a common petrogenetic process operating in terrestrial magma chambers that are mushy in nature (Lissenberg and MacLeod, 2016), and should be investigated further for potential influence on extraterrestrial magma evolution.

4.2.2 Flow of Melt to and from Mush: The Role of Mafic Recharge

RPF can cause melts to rise buoyantly through the crust, and additional mechanisms can work to destabilize this melt further. In particular, minerals with relatively primitive compositions are too refractory to be dissolved and "chemically excavated" by more evolved melts (Ubide and Kamber, 2018; Neave et al 2014), but relatively evolved grains can be more easily entrained from pre-existing shallower zones (i.e., Ganne et al., 2018). Mafic recharge is a particularly effective mechanism for defrosting, unlocking, and destabilizing mush and interstitial melt (Huber et al., 2011, Lissenberg and MacLeod, 2016, Sparks et al., 2019). Intruding primitive hot magma mixes with interstitial melt, and reacts with framework grains, unlocking them. By mixing with interstitial melt and (partly) dissolving framework grains, magma influx leads to homogenization of the melts ultimately derived from mushy lenses and erupted at the surface (i.e., Lissenberg et al., 2019). By unlocking mushes, a replenishing melt traveling through several lenses also has the potential to entrain diverse populations of phenocrysts and glomerocrysts (i.e., Lissenberg et al., 2019; Ubide and Kamber, 2018; Cashman et al. 2017). Dissolution of grains as a result of (mafic) recharge is commonly recognized as a process through which disequilibrium features can be generated (i.e., Ubide and Kamber., 2018). Introduction of primitive, hot magma carries with it a relative influx of MgO and Cr (for example), and can be coupled with disequilibrium features like resorption/dissolution. These textural and chemical features are observed in this study particularly with increased MgO and Sr contents in feldspar populations, and increased MgO, Cr, Sc in pyroxene, coupled with dissolution and sieving clearly seen in pyroxenes. Thus it is inferred that mafic recharge was also an important process in the evolution of lunar magmatic systems, and should be investigated further as a potential eruption trigger in extraterrestrial settings.

5 Conclusions

Altogether, this work indicates that lunar magmatic systems are more complex than previously thought, and carry distinct crystal cargoes which record distinct petrogenetic histories at the crystal scale. This is not unlike their terrestrial counterparts. This suggests that plumbing system architecture evolves similarly across rocky planetary bodies, and may operate similarly on other bodies where magmatism has operated previously or currently operates, including Mars, Venus, and Jupiter's moon Io (Wilson 2009, and references therein). We remind the reader that while the samples were chosen for their textural and chemical diversity for study here, they ultimately represent a random sampling of the mare basalt suite. Detailed investigations of each of the six magmatic systems studied here are warranted, along with detailed evaluations of other mare basalt suites, particularly those from other basalt-generating bodies where possible, in order to fully determine the exact plumbing system architecture and processes involved in magma petrogenesis across the Solar System.

6 Acknowledgements

First, we acknowledge the Apollo astronauts for collecting the lunar samples studied here, and all those involved in the Apollo program who made this possible. We also extend our thanks to Matt Duley at the Miami University Center for Advanced Microscopy and Imaging (CAMI) for his support during sample imaging, and Morgan Gillis from the Miami University Department of Geology and Environmental Earth Science (at the time of writing) for her help in carbon coating sample thin sections. This research was funded through a Geological Society of America Graduate Student Research Grant #13203-21 to AG.

7 Data Availability

Data is made available via a repository.

8 References

1. Basaltic Volcanism Study Project (BVSP) (1981) Basaltic Volcanism on the Terrestrial Planets. Pergamon Press, Inc., New York. 1286 pp.
2. Beattie, P. (1994) Systematics and energetics of trace-element partitioning between olivine and silicate melts: Implications for the nature of mineral/melt partitioning. Chemical Geology 117, 57-71.
3. Bennett, E. N., Lissenberg, C. J., Cashman, K. V. (2019) The significance of plagioclase textures in mid-ocean ridge basalt (Gakkel Ridge, Arctic Ocean). Contributions to Mineralogy and Petrology 174: 49. https://doi.org/10.1007/s00410-019-1587-1
4. Berlo, K., Blundy, J., Turner, S., Hawkesworth, C., 2007. Textural and chemical variation in plagioclase phenocrysts from the 1980 eruptions of Mount St. Helens, USA. Contrib. Mineral. Petrol. 154, 291–308.Bergantz et al., 2015
5. Bezard, R., Turner, S., Davidson, J., Schmitt, A.K., Lindsay, J., 2017. Origin and Evolution of Silicic Magmas in Oceanic Arcs; an in situ Study from St Lucia, Lesser Antilles. J. Petrol.58, 1279–1318.
6. Blundy J. D., Shimizu N. (1991) Trace element evidence for plagioclase recycling in calcalkaline magmas. Earth and Planetary Science Letters 102:2, 178-197.
7. Blundy, J. D., Wood, B. J. (1991) Crystal-chemical controls on the partitioning of Sr and Ba between plagioclase feldspar, silicate melts, and hydrothermal solutions. Geochimica et Cosmochimica Acta 55, 193-209.

8. Cashman K. V. (2015) Changing the paradigm – new views on magmatic systems provide new perspectives on volcanic processes. AGU, Fall Meeting 2015.
9. Cashman K. V., Sparks R. S. J., Blundy J. D. (2017) Vertically extensive and unstable magmatic systems: A unified view of igneous processes. Science 355, 6331. https://doi.org/10.1126/science.aag3055
10. Coish, R. A., Taylor, L. A. (1979) The Effects of Cooling Rate on Texture and Pyroxene Chemistry in DSDP LEG 34 Basalt: A Microprobe Study. Earth and Planetary Science Letters 42, 389-398.
11. Coote, A., Shane, P. (2018) Open-system magmatic behaviour beneath monogenetic volcanoes revealed by the geochemistry, texture and thermobarometry of clinopyroxene, Kaikohe-Bay of Islands volcanic field (New Zealand). Journal of Volcanology and Geothermal Research 368, 51-62. https://doi.org/10.1016/j.jvolgeores.2018.11.006
12. Costa, F., Morgan, D. (2011) Time Constraints from Chemical Equilibration in Magmatic Crystals. In: Dosseto, A., Turner, S. P., Van Orman, J. A. (Eds.) Timescales of Magmatic Processes: From Core to Atmosphere. Blackwell Publishing Ltd.
13. Couperthwaite, F. K., Thordarson, T., Morgan, D. J., Harvey, J., Wilson, M. (2020) Diffusion Timescales of Magmatic Processes in the Moinui Lava Eruption at Mauna Loa, Hawai'I, as Inferred from Bimodal Olivine Populations. Journal of Petrology 61 (7), egaa058. https://doi.org/10.1093/petrology/egaa058
14. Davidson J. P., Morgan D. J., Charlier B. L. A., Harlou R., Hora J. M. (2007) Microsampling and Isotopic Analysis of Igneous Rocks: Implications for the Study of Magmatic Systems. Annual Reviews in Earth and Planetary Science 35, 273-311. https://doi.org/10.1146/annurev.earth.35.031306.140211

15. Donohue P. H., Neal C. R. (2015) Quantitative textural analysis of ilmenite in Apollo 17 high titanium mare basalts. Geochimica et Cosmochimica Acta 149, 115-130. https://doi.org/10.1016/j.gca.2014.11.002

16. Edmonds, M., Cashman, K. V., Holness, M., Jackson, M. (2019) Architecture and dynamics of magma reservoirs. Philosophical Transactions of the Royal Society A, 377: 20180298. http://dx.doi.org/10.1098/rsta.2018.0298

17. Gawronska, A. J., McLeod, C. L., Blumenfeld, E. H., Hanna, R. D. Zeigler, R. A. (2022) New interpretations of lunar mare basalt flow emplacement from XCT analysis of Apollo samples. Icarus 388, 115216. https://doi.org/10.1016/j.icarus.2022.115216.

18. Ginibre C., Worner G., Kronz A. (2007) Crystal Zoning as an Archive for Magma Evolution. Elements 3, 261-266. https://doi.org/10.2113/gselements.3.4.261

19. Grove, T. L., Baker, M. B., Kinzler, R. J. (1984) Coupled CaAl-NaSi diffusion in plagioclase feldspar: Experiments and applications to cooling rate speedometry. Geochimica et Cosmochimica Acta 48, 2113-2121.

20. Hart, S. R., Dunn, T. (1993) Experimental cpx/melt partitioning of 24 trace elements. Contributions to Mineralogy and Petrology 113, 1-8.

21. Head, J. W., (1976) Lunar volcanism in space and time. Reviews of Geophysics 14 (2), 265-300.

22. Higgins M. D. (2000) Measurement of crystal size distributions. American Mineralogist 85, 1105-1116. https://doi.org/10.2138/am-2000-8-901

23. Higgins M. D., Roberge J. (2007) Three magmatic components in the 1973 eruption of Eldfell volcano, Iceland: Evidence form plagioclase crystal size distribution (CSD) and geochemistry.

Journal of Volcanology and Geothermal Research 161:3, 247-60. https://doi.org/10.1016/j.jvolgeores.2006.12.002

24. Jackson M, Blundy J, Sparks RSJ. 2018 Chemical differentiation, cold storage and remobilization of magma in the Earth’s crust. Nature 355, eaag3055. doi:10.1038/s41586-018-0746-2
25. Jerde E. A., Snyder G. A., Taylor L. A., Liu Y.-G., Schmitt R. A. (1994) The origin and evolution of lunar high-Ti basalts: Periodic melting of a single source at Mare Tranquilitatis. Geochimica et Cosmochimica Acta 58, 515-527. https://doi.org/10.1016/0016-7037(94)90480-4
26. Jerram D. A., Davidson J. P. (2007) Frontiers in Textural and Microgeochemical Analysis. Elements 3:4, 235-238. https://doi.org/10.2113/gselements.3.4.235
27. Kent, A. J. R., Darr, C., Koleszar, A. M., Salisbury, M. J., Cooper, K. M. (2010) Preferential eruption of andesitic magmas through recharge filtering. Nature Geoscience 3, 631-636. https://doi.org/10.1038/ngeo924
28. Lee C-T. A., Luffi P., Plank T., Dalton H., Leeman W. P. (2009) Constraints on the depths and temperatures of basaltic magma generation on Earth and other terrestrial planets using new thermobarometers for mafic magmas. Earth and Planetary Science Letters 279:1-2, 20-33. https://doi.org/10.1016/j.epsl.2008.12.020
29. Lindstrom, M. M., Haskin, L. A. (1978) Causes of compositional variations within mare basalt suites. Proceedings of the 9th Lunar and Planetary Science Conference, 465-486.
30. Lissenberg, C. J., MacLeod, C. J. (2016) A Reactive Porous Flow Control on Mid-ocean Ridge Magmatic Evolution. Journal of Petrology 57 (11&12), 2195-2220. https://doi.org/10.1093/petrology/egw074

31. Lissenberg, C. J., MacLeod, C. J., Bennett, E. N. (2019) Consequences of a crystal mush-dominated magma plumbing system: a mid-ocean ridge perspective. Philosophical Transactions of the Royal Society A 377: 20180014. http://dx.doi.org/10.1098/rsta.2018.0014

32. Lofgren, G., Donaldson, C. H., Williams, R. J., Mullins Jr., O., Usselman, T. M. (1974) Experimentally reproduced textures and mineral chemistry of Apollo 15 quartz normative basalts. Proceedings of the Fifth Lunar Conference 5 (1), 549-567.

33. Marsh B. D. (2009) Dynamics of Magmatic Systems. Elements 2:5, 287-292. https://doi.org/10.2113/gselements.2.5.287

34. McKenzie, D. (1984) The Generation and Compaction of Partially Molten Rock. Journal of Petrology 25 (3), 713-765.

35. McLeod, C. L., and Gawronska, A. J. (in press) The Lunar Mantle. In: Cudnik, B. (Eds.) The Encyclopedia of Lunar Science. Springer, Cham.

36. Meyer, C., 2016. The Lunar Sample Compendium Database. Astromaterials Research and Exploration Science. https://curator.jsc.nasa.gov/lunar/lsc/

37. Middlemost E. A. K. (2014) Magmas, Rocks and Planetary Development. Routlege, London. 324 pp

38. Mollo, S., Putirka, K., Iezzi, G., Del Gaudio, P., Scarlato, P. (2011) Plagioclase-melt (dis)equilibrium due to cooling dynamics: Implications for thermometry, barometry, and hygrometry. Lithos 125, 221-235. doi:10.1016/j.lithos.2011.02.008

39. Moore, A., Coogan, L. A., Costa, F., Perfit, M. R. (2014) Primitive melt replenishment and crystal-mush disaggregation in the weeks preceding the 2005-2006 eruptions 9°50'N, EPR. Lithos 403 (15-26). https://doi.org/10.1016/j.epsl.2014.06.015

40. Morgan D. J., Jerram D. A. (2006) On estimating crystal shape for crystal size distribution analysis. Journal of Volcanoly and Geothermal Research 154, 1-7. https://doi.org/10.1016/j.jvolgeores.2005.09.016

41. National Research Council (2007) The Scientific Context for Exploration of the Moon. Washington, DC: The National Academies Press. https://doi.org/10.17226/11954.

42. Neal, C. R., Taylor L. A. (1992) Petrogenesis of mare basalts: A record of lunar volcanism. Geochimica et Cosmochimica Acta 56, 2177-2211.

43. Neal, C. R., Hacker, M. D., Snyder, G. A., Taylor, L. A., Liu, Y.-G., Schmitt , R. A. (1994) Basalt generation at the Apollo 12 site: Part 1: New data, classification, and re-evaluation. Meteoritics 29, 334-348.

44. Neal C. R., Donohue P., Fagan A. L., O'Sullivan K., Oshrin J., Roberts S. (2015) Distinguishing between basalts produced by endogenic volcanism and impact processes: A non-destructive method using quantitative petrography of lunar basaltic samples. Geochimica et Cosmochimica Acta 148, 6280. https://doi.org/10.1016/j.gca.2014.08.020

45. Neave, D. A., Maclennan, J., Hartley, M. E., Edmonds, M. & Thordarson, T. (2014) Crystal storage and transfer in basaltic systems: the Skuggafjöll eruption, Iceland. J. Petrol. 55, 2311–2346 (2014)

46. Neave, D. A., MacIennan J. (2020) Clinopyroxene Dissolution Records Rapid Magma Ascent. Frontiers in Earth Science 8, 188. doi: 10.3389/feart.2020.00188

47. Neave, D. A., Beckmann, P., Behrens, H., Holtz, F. (2021) Mixing between chemically variable primitive basalts creates and modifies crystal cargoes. Nature Communications 12, 5492. https://doi.org/10.1038/s41467-021-25820-z

48. Nyquist, L. E., Wooden, J. L., Shih, C.-Y., Wiesmann, H., Bansal, B. M. (1981) Isotopic and REE studies of lunar basalt 12038: implications for petrogenesis of aluminous mare basalts. Earth and Planetary Science Letters 55, 335-355.

49. Ogawa M. (2018) Magmatic differentiation and convective stirring of the mantle in early planets: the effects of the magmatism-mantle upwelling feedback. Geophysical Journal International 215:3, 2144-2155. https://doi.org/10.1093/gji/ggy413

50. Paces, J. B., Nakai, S., Neal, C. R., Taylor, L. A., Halliday, A. N., Lee, D.-C. (1991) A strontium and neodymium isotopic study of Apollo 17 high-Ti mare baslts: Resolution of ages, evolution of magmas, and origins of source heterogeneities. Geochimica et Cosmochimica Act 55, 2025-2043.

51. Papike, J. J., Hodges, F. N., Bence, A. E., Cameron, M., Rhodes, J. M. (1976) Mare Basalts: Crystal Chemistry, Mineralogy, and Petrology. Reviews of Geophysics and Space Physics 14 (4), 475-540.

52. Paulatto, M., Hooft, E. E., Chrapkiewicz, K., Heath, B., Toomey, D. R., Morgan, J. V. (2022) Advances in seismic imaging of magma and crystal mush. Frontiers in Earth Science 10. https://doi.org/10.3389/feart.2022.970131

53. Qian, Y., Xiao, L., Wang, Q., Head, J. W., Yang, R., Kang, Y., van der Bogert, C. H., Hiesinger, H., Lai, X., Wang, G., Pang, Y., Zhang, N., Yuan, Y., He, Q., Huang, J., Zhao, J., Wang, J., Zhao, S. (2021) China;s Chang'e-5 landing site: Geology, stratigraphy, and provenance of materials. Earth and Planetary Science Letters 561, 116855. https://doi.org/10.1016/j.epsl.2021.116855

54. Richter FM, McKenzie D. (1984) Dynamical models for melt segregation from a deformable matrix. J. Geol. 92, 729–740. (doi:10.1086/628908)

55. Ryder, G., Schuraytz, B. C. (2001) Chemical variation of the large Apollo 15 olivine-normative mare basalt rock samples. Journal of Geophysical Research 106 (E1), 1435-1451.

56. Salisbury, M. J., Bohrson, W. A., Clynne, M. A., Ramos, F. C., Hoskin, P. (2008) Multiple Plagioclase Crystal Populations Identified by Crystal Size Distribution and *in situ* Chemical Data: Implications for Timescales of Magma Chamber Processes Associated with the 1915 Eruption of Lassen Peak, CA. Journal of Petrology 49 (10), 1755-1780. doi:10.1093/petrology/egn045

57. Schleicher J, Bergantz G. (2017) The mechanics and temporal evolution of an open-system magmatic intrusion into a crystal-rich magma. J. Petrol. 58, 1059–1072. doi:10.1093/petrology/egx045

58. Schneider, C. A., Rasband, W. S., Eliceiri, K. W., (2012). NIH Image to ImageJ: 25 years of image analysis. Nature methods 9(7), 671-675, doi: 10.1038/nmeth.2089

59. Shearer, C. K., Hess, P. C., Wieczorek, M. A., Pritchard, M. E., Parmentier, E. M., Borg, L. E., Longhi, J., Elkins-Tanton, L. T., Neal, C. R., Antonenko, I., Canup, R. M., Halliday, A. N., Grove, T. L., Hager, B.H., Lee, D-C., Wiechert, U., 2006. Thermal and Magmatic Evolution of the Moon, in: Jollif, B. L., Wieczorek, M. A., Shearer, C. K., Neal, C. R., eds., New Views of the Moon. Reviews in Mineralogy & Geochemistry 60(1), 365-518, doi:10.2138/rmg.2006.60.4

60. Solano, J. M. S., Jackson, M. D., Sparks, R. S. J., Blundy, J. (2014) Evolution of major and trace element composition during melt migration through crystalline mush: Implications for chemical differentiation in the crust. American Journal of Science 314 (5), 895-939. https://doi.org/10.2475/05.2014.01

61. Sparks, R. S. J., Annen, C., Blundy, J. D., Cashman, K. V., Rust, A. C., Jackson, D. (2019) Formation and dynamics of magma reservoirs. Philosophical Transactions of the Royal Society A 377, 20180019. http://dx.doi.org/10.1098/rsta.2018.0019
62. Spera, F. J., Bohrson, W. A. (2018) Rejuvenation of crustal magma mush: A tale of multiply nested processes and timescales. American Journal of Science 318 (1), 90-140. https://doi.org/10.2475/01.2018.05
63. Spudis, P. D., McGovern, P. J., Kiefer, W. S. (2013) Large shield volcanoes on the Moon. Journal of Geophysical Research: Planets 118 (5), 1063-1081. https://doi.org/10.1002/jgre.20059
64. Stooke, P. J. (2017) Luna Missions. In: Cudnik, B. (eds) Encyclopedia of Lunar Science. Springer, Cham. https://doi.org/10.1007/978-3-319-05546-6_97-1
65. Streck, M. J. (2008) Mineral Textures and Zoning as Evidence for Open System Processes. Reviews in Mineralogy and Geochemistry 69, 595-622. https://doi.org/10.2138/rmg.2008.69.15
66. Sun, S.-s., McDonough, W. F. (1989) Chemical and isotopic systematics of oceanic basalts: implications for mantle composition and processes. In: Saunders, A. D., Norry, M. J. (Eds.) Magmatism in the Ocean Basins. Geological Society Special Publications 42, 313-345 pp.
67. Ubide T., Gale C., Larrea P., Arranz E., Lago M., Tierz P. (2014) The Relevance of Crystal Transefer to Magma Mixing: A Case Study in Composite Dykes from the Central Pyrenees. Journal of Petrology 55:8, 1535-1559. https://doi.org/10.1093/petrology/egu033
68. Ubide, T., Kamber, B. S. (2018) Volcanic crystals as time capsules of eruption history. Nature Communications 9: 326. https://doi.org/10.1038/s41467-017-02274-w

69. Ubide, T., Caulfield, J., Brandt, C., Bussweiler, Y., Mollo, S., Di Stefano, F., Nazzari, M., Scarlato, P. (2019) Deep Magma Storage Revealed by Multi-Method Elemental Mapping of Clinopyroxene Megacrysts at Stromboli Volcano. Frontiers in Earth Science 7:239. doi: 10.3389/feart.2019.00239

70. Ustunisik, G., Kilinc, A., Nielsen, R. L. (2014) New insights into the processes controlling compositional zoning in plagioclase. Lithos 200-201, 80-93. http://dx.doi.org/10.1016/j.lithos.2014.03.021

71. Velázquez Santana, L. C., McLeod, C. L., Blakemore, D., Shaulis, B., Hill, T. (2020) Bolivian hornblendite cumulates: Insights into the depths of Central Andean arc magmatic systems. Lithos 370-371, 105618. https://doi.org/10.1016/j.lithos.2020.105618

72. Vernon, R. H., 2018. A Practical Guide to Rock Microstructure, 2nd edition. Cambridge University Press, Cambridge. doi: 10.1017/9781108654609

73. Vetter, S. K., Shervais, J. W., Lindstrom, M. M. (1988) Petrology and Geochemistry of Olivine-Normative and Quartz-Normative Basalts from Regolith Breccia 15498: New Diversity in Apollo 15 Mare Basalts. Proceedings of the 18th Lunar and Planetary Science Conference

74. Whitford-Stark, J. L. (1982) Factors influencing the morphology of volcanic landforms: An earth-moon comparison. Earth-Science Reviews 18 (2), 109-168. https://doi.org/10.1016/0012-8252(82)90050-2

75. Wilding, J. D., Zhu, W., Ross, Z. E., Jackson, J. M. (2023) The magmatic web beneath Hawai'i. Science 379, 462-468. https://doi.org/10.1126/science.ade5755

76. Wilson, L. (2009) Volcanism in the Solar System. Nature Geoscience 2, 389-397. https://doi.org/10.1038/ngeo529

77. Yang, H. and Zhao, W. (2018) Apollo Program. In: Cudnik, B. (eds) Encyclopedia of Lunar Science. Springer, Cham. https://doi.org/10.1007/978-3-319-05546-6_101-1

78. Zellmer, G. (2021) Gaining acuity on crystal terminology in volcanic rocks. Bulletin of Volcanology 83:77. https://doi.org/10.1007/s00445-021-01505-9

79. Zhou, Q. (2017) Lunar Meteorites. In: Cudnik, B. (Eds.) Encyclopedia of Lunar Science. Springer, Cham. https://doi.org/10.1007/978-3-319-05546-6_58-1

9. Supplemental figures

Table S1: Summary of sample characteristics.

Sample	Sampling Location	Dominant Texture	Major Composition	Trace Composition
10057	Mare Tranquilitatis	Fine grained	High Ti	REE enriched
12038	Oceanus Procellarum	Medium grained	Low Ti	not REE enriched
12043	Oceanus Procellarum	Porphyritic	Low Ti	not REE enriched
15085	Mare Imbrium	Coarse grained	Low Ti	not REE enriched
15556	Mare Imbrium	Fine grained	Low Ti	not REE enriched
70017	Mare Serenitatis	Medium grained	High Ti	not REE enriched

Table S2: Summary of plagioclase feldspar CSD parameters plotted in Fig. 4c.

Sample	Slope	Interept
10057	-8.7455	7.7511
12038	-1.0415	2.7218
12043	-1.4895	3.9257
15556,241	-5.2626	5.3809
70017	-2.9172	3.1679

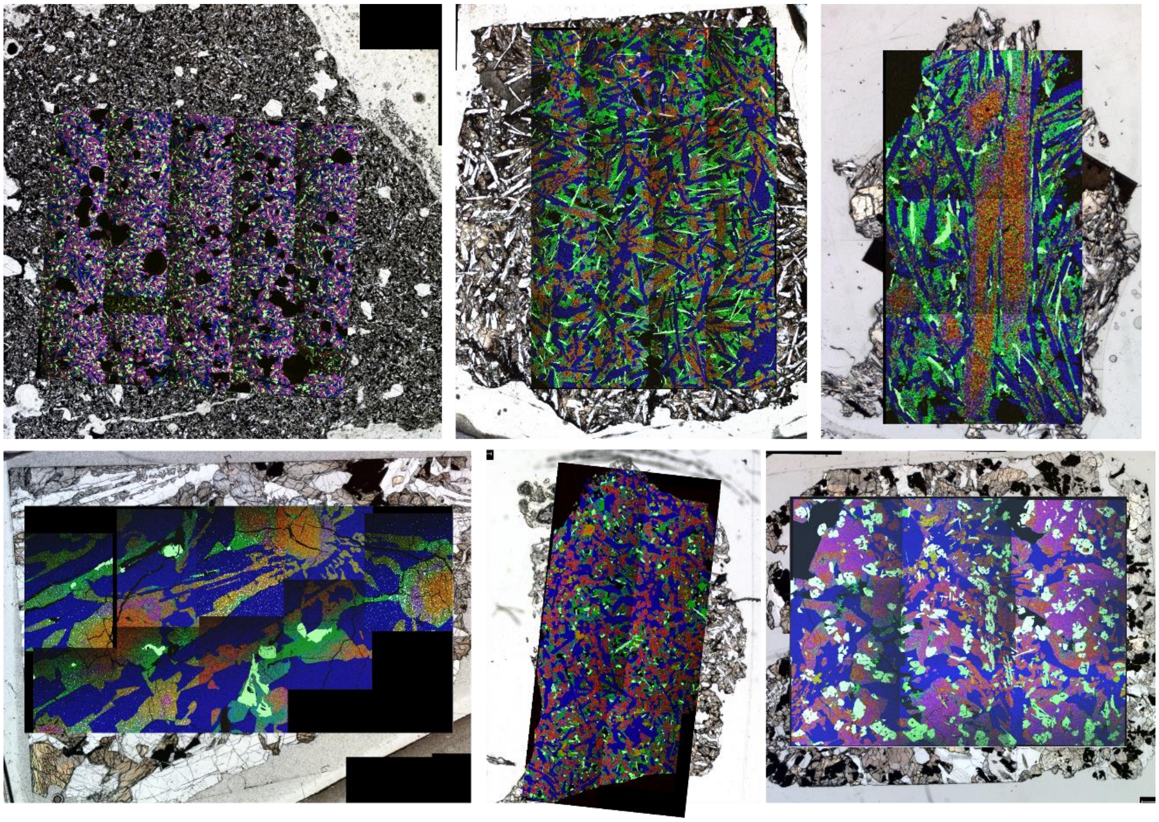

Fig. S1: SEM-EDS major elements maps overlying plane-polarized light images: red is Mg, green is Fe, blue is Ca, white is Ti.

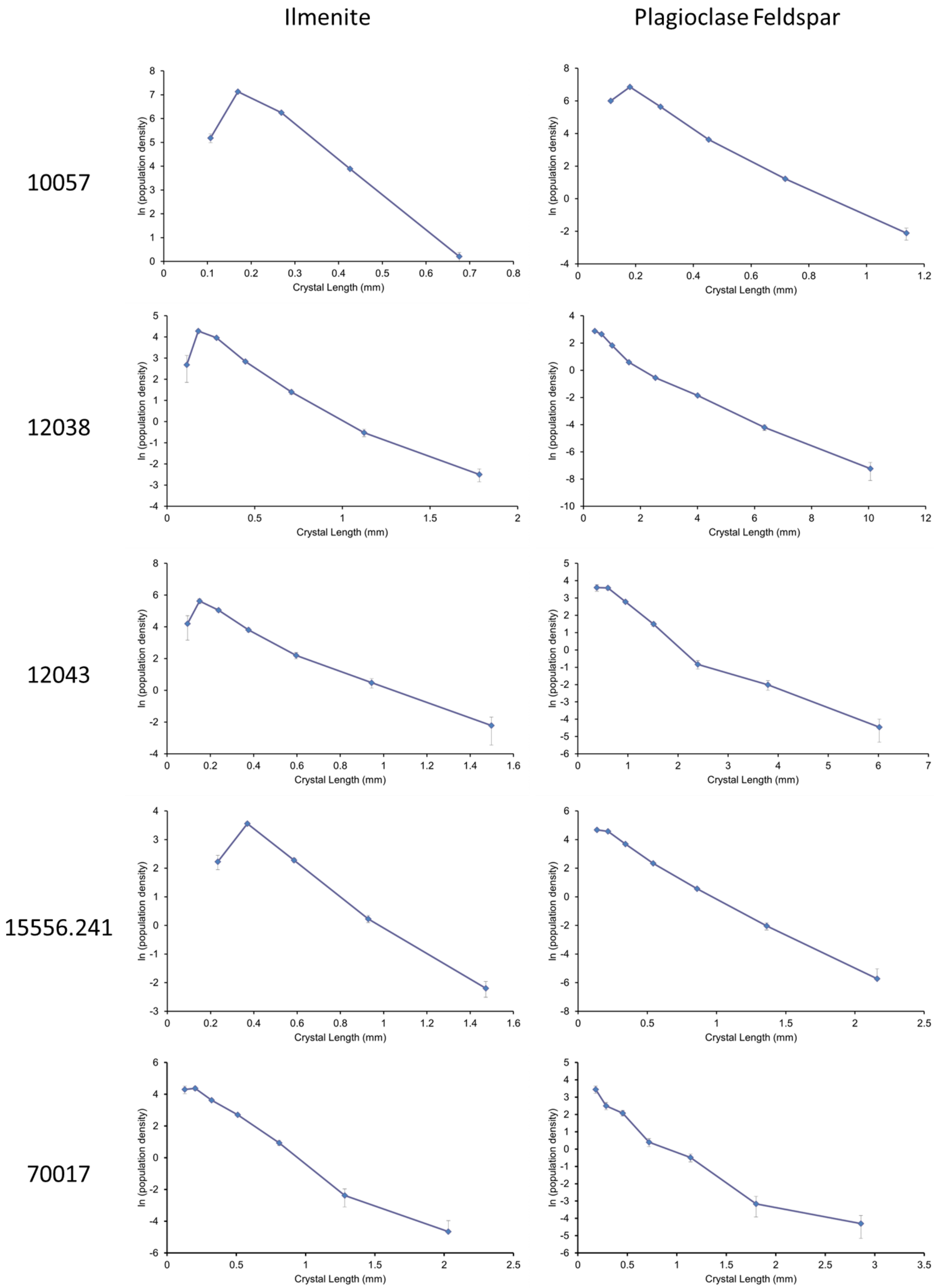

Fig. S2: Individual CSD plots for ilmenite and plagioclase feldspar in these samples.

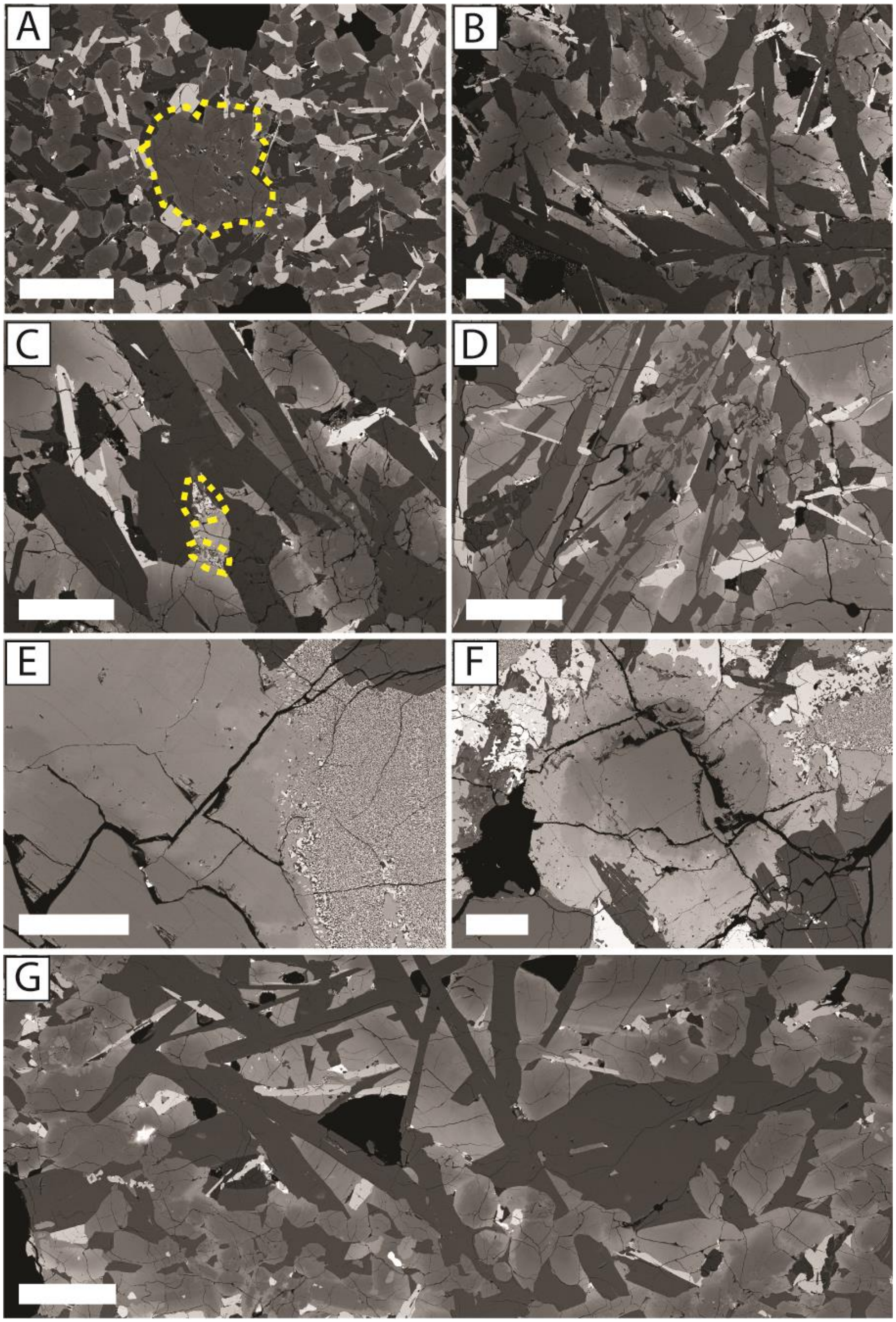

Fig. S3: Exemplary grain textures in the studied samples; all scalebars are 250 µm. A) Glomerocryst in 10057. B) Plagioclase subophitically enclosed in pyroxene in 12038. C) Symplectite along pyroxene rims in 12038. D) Pyroxene and feldspar matrix in 12043. E) Replacement of pyroxene by symplectite in 15085. F) Pyroxene with distinct zoning in 15085. G) Plagioclase feldspar clots in 15556 at top of the image – compared to interstitial texture of feldspar seen at the bottom of the image, typical of this sample.

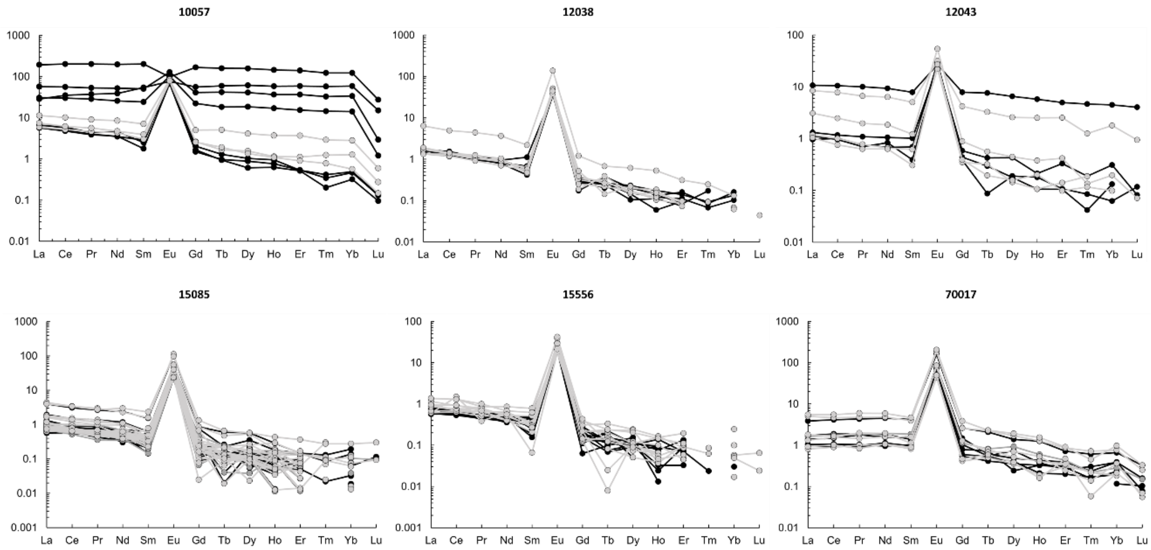

Fig. S4: Chondrite-normalized spidergrams of plagioclase feldspar analyses across the samples studied. Cores in black, rims in light gray.

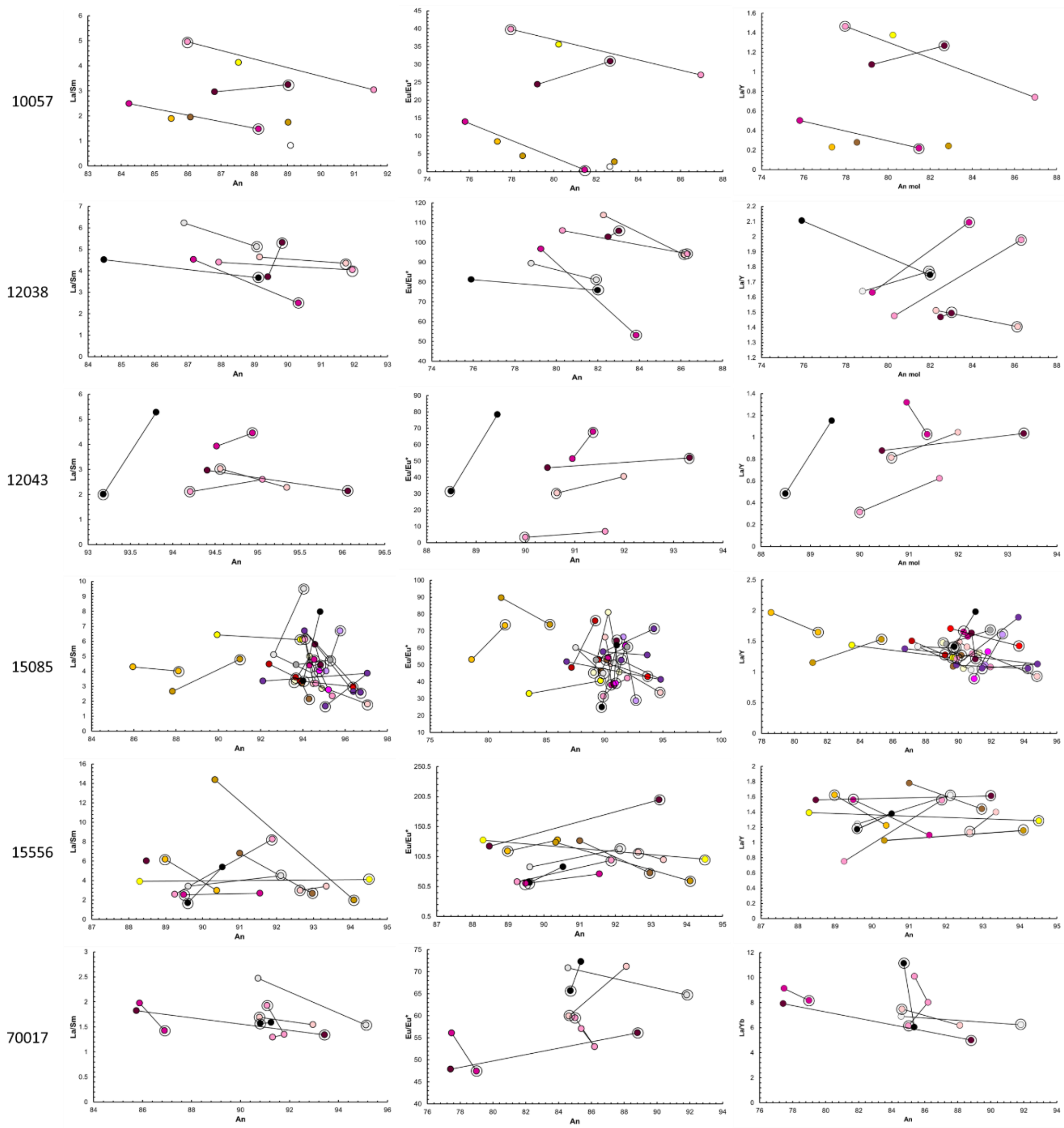

Fig. S5: Trace element ratios in plagioclase feldspar grains studied here. Graphs match color scheme of Figs. 5 and 6.

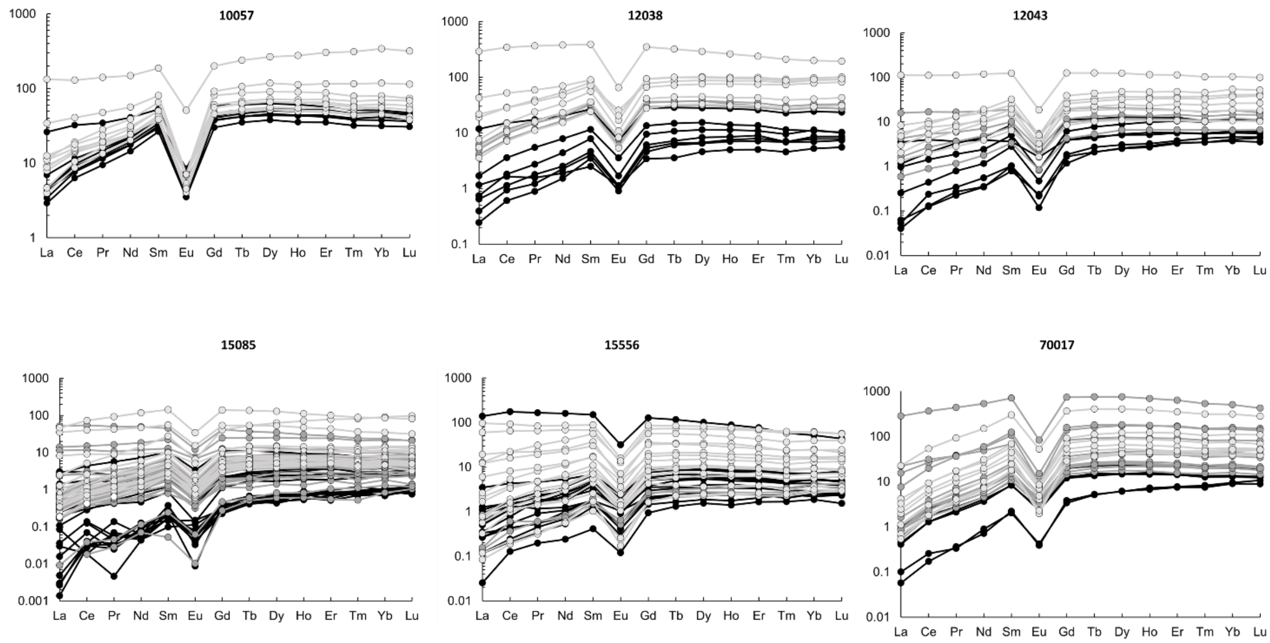

Fig. S6: Chondrite-normalized spidergrams of pyroxene analyses across the samples studied. Core analyses are in black, mantles in dark gray, and rims in light gray.

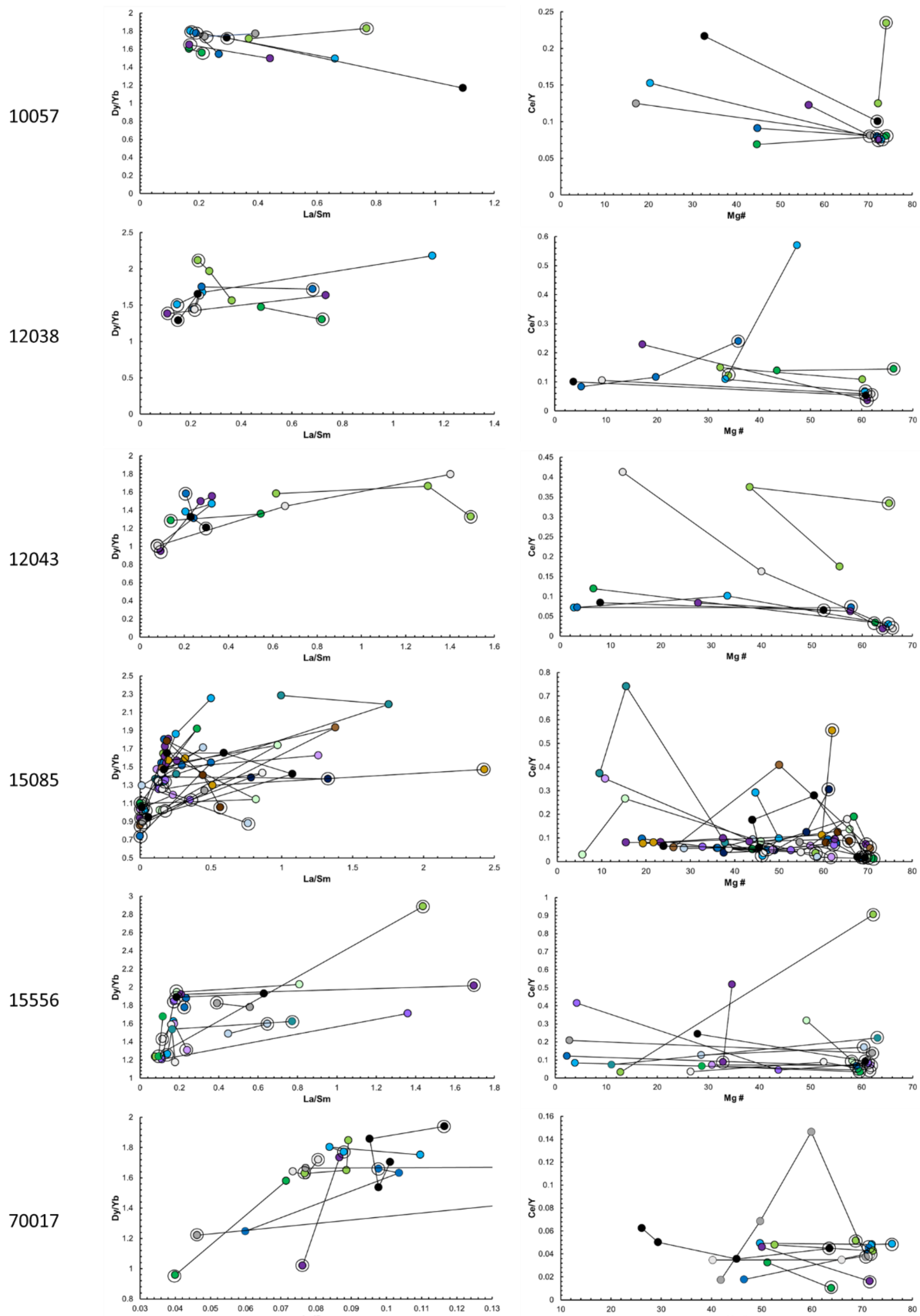

Fig. S7: Trace element ratios in pyroxene grains studied here. Graphs match color scheme of Figs. 7 and 8.

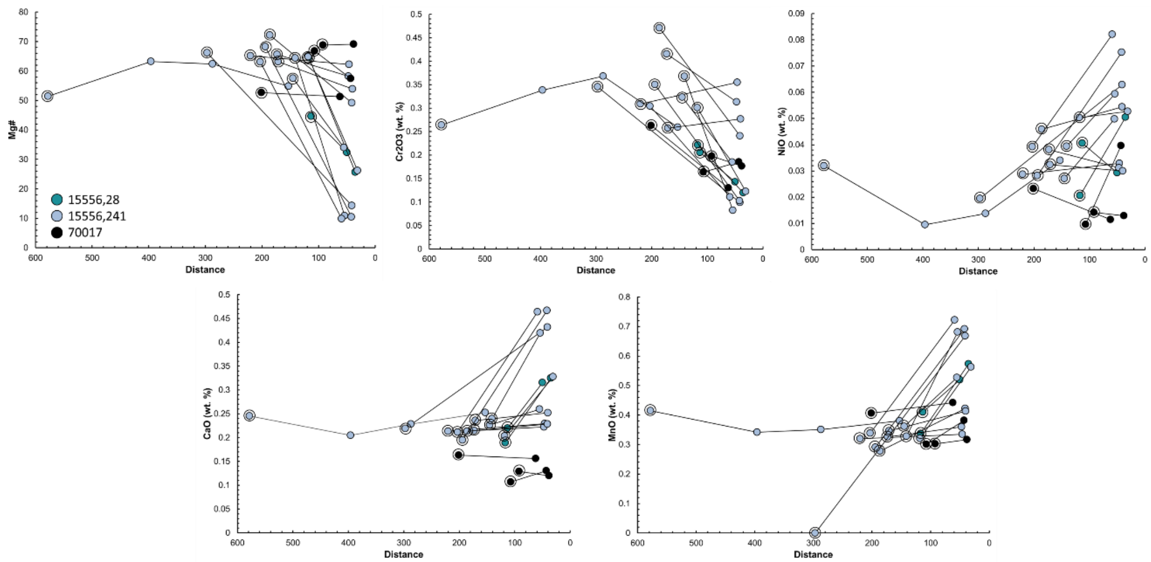

Fig. S8: Major and minor element data for olivine grains studied here. Encircled points mark the core of each grain.